Mon. Not. R. Astron. Soc. **000**, 000–000 (0000) Printed 1 February 2008 (MN LATEX style file v1.4)

Cosmic Confusion: Degeneracies among Cosmological Parameters Derived from Measurements of Microwave Background Anisotropies

G. Efstathiou[1] and J.R. Bond[2]
[1] *Institute of Astronomy, Madingley Road, Cambridge, CB3 OHA.*
[2] *CITA, 60 St. George St., University of Toronto, Toronto ON M5S 3H8, Canada.*

arXiv:astro-ph/9807103v1 10 Jul 1998

1 February 2008

ABSTRACT
In the near future, observations of the cosmic microwave background (CMB) anisotropies will provide accurate determinations of many fundamental cosmological parameters. In this paper, we analyse degeneracies among cosmological parameters to illustrate some of the limitations inherent in CMB parameter estimation. For simplicity, throughout our analysis we assume a cold dark matter universe with power-law adiabatic scalar and tensor fluctuation spectra. We show that most of the variance in cosmological parameter estimates is contributed by a small number (two or three) principal components. An exact likelihood analysis shows that the usual Fisher matrix approach can significantly overestimate the errors on cosmological parameters. We show that small correlated errors in estimates of the CMB power spectrum at levels well below the cosmic variance limits, (caused, for example, by Galactic foregrounds or scanning errors) can lead to significant biases in cosmological parameters. Estimates of cosmological parameters can be improved very significantly by applying theoretical restrictions to the tensor component and external constraints derived from more conventional astronomical observations such as measurements of he Hubble constant, Type 1a supernovae distances and observations of galaxy clustering and peculiar velocities.

1 INTRODUCTION

A number of investigations have shown that high precision measurements of the cosmic microwave background (CMB) anisotropies can be used to determine many cosmological parameters to unprecedented precision (Jungman *et al.* 1996; Bond, Efstathiou and Tegmark 1997, hereafter BET97; Zaldarriaga, Spergel and Seljak 1997, hereafter ZSS97). These parameters include the amplitudes and spectral indices of the scalar and tensor fluctuations predicted by inflationary models (*e.g.* Knox and Turner 1994, Knox 1995, Lidsey *et al.* 1997, Souradeep *et al.* 1998, Copeland *et al.* 1998), the densities of the various components of the mass density of the Universe, and constraints on the geometry of the Universe.

The prospect of measuring such cosmological parameters to high precision has formed an important part of the scientific case for two approved satellite missions, NASA's MAP satellite (Bennett *et al.* 1996) and ESA's Planck Surveyor*(Bersanelli *et al.* 1996). In addition, ground based and balloon experiments are already beginning to set useful constraints on some of these parameters (*e.g.* Bond and Jaffe 1997, Hancock *et al.* 1997, Lineweaver and Barbosa 1998a,b, Webster *et al.* 1998).

In this paper, we investigate degeneracies among cosmological parameters, *i.e.* to what extent can we disentangle one parameter from another using measurements of the CMB anisotropies alone (see also Bond *et al.* 1994). We assume throughout that the primordial fluctuations are adiabatic and Gaussian, as expected in most inflationary models (*e.g.* Linde 1990). These assumptions are physically well motivated and allow accurate calculations of the CMB anisotropies as a function of cosmological parameters via fast numerical solutions of the relativistic Boltzmann equation. The accuracy of computations of CMB anisotropies in topological defect models has greatly improved recently (see Turok, Pen and Seljak, 1997, Albrecht, Battye and Robinson 1997) and tend to disfavour the simplest versions of defect models. However, these calculations cannot yet be done to sufficient precision for the type of analysis presented in this paper. Nevertheless, some qualitative features of the discussion presented here are likely to be applicable to defect models and to other classes of models such as isocurvature theories.

We distinguish between a nearly exact degeneracy (which we call the 'geometrical' degeneracy) and other parameter degeneracies. The geometrical degeneracy (BET97, ZSS97) leads to near identical CMB anisotropies in universes with different background geometries but identical

* Formerly known as COBRAS/SAMBA

© 0000 RAS

matter content. In linear perturbation theory, observations of the primary CMB anisotropies cannot break the geometrical degeneracy, no matter how precise the experimental measurements. The geometrical degeneracy thus imposes fundamental limits on measurements of the curvature of the Universe and the Hubble constant derived from CMB anisotropy measurements. Of the remaining parameter degeneracies, some are extremely sensitive to the accuracy of the CMB anisotropy measurements whilst others are not. In this paper, we give a physical description of the causes of some of the parameter degeneracies and of the fundamental limits imposed by CMB anisotropy measurements.

This paper is laid out as follows. In Section 2 we summarise the formalism based on the Fisher matrix (Jungman *et al.* 1996, Tegmark, Taylor and Heavens 1997) which is assumed in most discussions of parameter estimation from the CMB. Throughout this paper, we use approximate experimental parameters for the MAP and Planck satellites to provide numerical examples of what might be achieved in the next decade or so. The experimental parameters that we use are summarised in Section 2. In Section 3, we discuss the geometrical degeneracy and we show that with an appropriate change of variables, the Fisher matrix can be applied to give accurate results for cosmological models of arbitrary curvature. In Section 4, we specialise to spatially flat cosmological models and analyse degeneracies among other cosmological parameters. We show that a principal component analysis provides a powerful technique for analysing degeneracies among parameters. For experiments such as MAP and Planck, that sample the CMB anisotropy power spectrum beyond the first Doppler peak, the first few principal components dominate the expected variances of most cosmological parameters. We test the accuracy of the Fisher matrix approach by performing an exact likelihood analysis in a subspace defined by the two most poorly determined principal components. Some of the degeneracies among cosmological parameters can be understood in terms of the locations of the Doppler peaks and of the height of the first Doppler peak. In Section 4, we compare the accuracies of parameter estimates from the improved version of MAP with those from Planck. We distinguish between 'strength' and 'statistical significance' in the analysis of CMB power spectra and discuss the effects of possible systematic errors that might arise, for example, through inaccurate subtraction of point sources, Galactic foregrounds and map reconstruction errors.

Section 5 discusses briefly how some of the degeneracies among cosmological parameters can be removed by using other types of observation, *e.g.* measurements of the Hubble constant, the age of the Universe and constraints on the luminosity distance from observations of distant Type 1a supernovae. Our conclusions are summarised in Section 6. Throughout this paper we use CMB power spectra computed with the CMBFAST code developed by Seljak and Zaldarriaga (1996).

2 FISHER MATRIX AND EXPERIMENTAL PARAMETERS

We assume that the initial fluctuations are adiabatic and Gaussian. The temperature anisotropies $\Delta T/T$ of the CMB on the celestial sphere can be decomposed in a spherical harmonic expansion,

$$\frac{\Delta T}{T} = \sum_{\ell,m} a_{\ell,m} Y_\ell^m(\theta,\phi)\,, \tag{1}$$

where each coefficient $a_{\ell,m}$ is statistically independent and Gaussian distributed with zero mean and variance

$$C_\ell = \langle |a_{\ell,m}|^2 \rangle\,. \tag{2}$$

The power spectrum, C_ℓ, completely specifies the statistical properties of the primary CMB temperature fluctuations if the initial fluctuations are Gaussian. The anisotropy of Thomson scattering results in a small net linear polarization of the CMB anisotropies (Kaiser 1983, Bond and Efstathiou 1984). For near scale-invariant spectra, this linear polarization amounts to a few percent of the total temperature anisotropy and should be measurable in future CMB experiments such as MAP and Planck. Polarization introduces three additional power-spectra to fully characterise the temperature anisotropies. These define the 'electric' and 'magnetic' components of the polarization pattern and the cross correlation of the polarization pattern with the temperature anisotropies (see e.g. Seljak and Zaldarriaga 1996, Hu and White 1997). We do not analyse polarization in any detail in this paper. The effects of polarization measurements on cosmological parameters has been discussed recently by ZSS97. Their results show that polarization measurements can improve the accuracy of most cosmological parameters by relatively modest factors, with two important exceptions, distinguishing between scalar and tensor modes and determining the redshift at which the intergalactic medium was reionized. The role of polarization will be discussed further in Section 4.

We follow the notation of BET97 and assume that a cosmological model is specified by a set of parameters $\mathbf{s}$. Let $P(\mathbf{s}|prior)$ be the prior probability distribution of the parameters $\mathbf{s}$ and $\mathcal{L}(\mathbf{s})$ the likelihood function defined by the experiment. The probability distribution of the parameters $\mathbf{s}$, taking into account the new experimental information, is given by Bayes theorem $P(\mathbf{s}) \propto \mathcal{L}(\mathbf{s})P(\mathbf{s}|prior)$. If the errors $\Delta\mathbf{s} \equiv \mathbf{s}-\mathbf{s}_0$ about the target model parameters $\mathbf{s}_0$ are small, an expansion of $\ln\mathcal{L}$ to quadratic order about the maximum leads to the expression,

$$\mathcal{L} \approx \mathcal{L}_m \exp\left[-\frac{1}{2}\sum_{ij} F_{ij}\delta s_i \delta s_j\right] \tag{3}$$

where F_{ij} is the Fisher matrix, given by derivatives of the CMB power spectrum with respect to the parameters $\mathbf{s}$

$$F_{ij} = \sum_\ell \frac{1}{(\Delta \mathrm{C}_\ell)^2}\frac{\partial \mathrm{C}_\ell}{\partial s_i}\frac{\partial \mathcal{C}_\ell}{\partial s_j}. \tag{4}$$

The quantity ΔC_ℓ in equation 4 is the standard error on the estimate of C_ℓ. For an experiment with N frequency channels (denoted by subscript c), angular resolution $(\theta_c)_{fwhm}$ and sensitivity $(\sigma_c)_{pix}$ per resolution element ($(\theta_c)_{fwhm} \times (\theta_c)_{fwhm}$ pixel) sampling a fraction f_{sky},

$$(\Delta \mathrm{C}_\ell)^2 \approx \frac{2}{(2\ell+1)f_{sky}}\left(\mathrm{C}_\ell + \overline{w}^{-1}\overline{\mathcal{B}}_\ell^{-2}\right)^2, \tag{5a}$$

$$\overline{w} \equiv \sum_c w_c, \quad \overline{\mathcal{B}}_\ell^2 \equiv \sum_c \mathcal{B}_{c\ell}^2 w_c/\overline{w}, \tag{5b}$$

$$w_c \equiv (\sigma_{c,pix}\theta_{c,pix})^{-2}, \quad \mathcal{B}_{c\ell}^2 \approx e^{-\ell(\ell+1)/\ell_s^2}, \tag{5c}$$

(see Knox 1995 and BET97), where we have assumed that the experimental beam profile $\mathcal{B}_c$ is Gaussian with width $\ell_s \equiv \sqrt{8\ln 2}(\theta_c)_{fwhm}^{-1}$. If we assume a uniform prior, as we will do throughout this paper, then the covariance matrix $\mathbf{M} \equiv \langle \delta s \delta s^\dagger \rangle$ is the inverse of the Fisher matrix $\mathbf{F}$. The standard deviation of a parameter s_i, marginalized over uncertainties in the other parameters, is given by $\sigma_i = M_{ii}^{1/2}$.

Table 2 lists the resolutions, θ_{fwhm}, sensitivities σ_{pix} and the noise power parameters w^{-1} for the various frequency channels that we have adopted. The parameter set labelled OMAP ('original MAP') is for the original specifications of the MAP satellite, as given in the proposal of Bennet *et al.* Parameters for the current MAP design are listed under the heading CMAP ('current MAP'). These include a significant improvement in the angular resolution at all frequencies compared to the original design specifications. We have listed the parameters for the 40, 60 and 90 GHz channels; the angular resolutions of the lower frequency MAP channels are so much poorer (0.93° at 22GHz and 0.68° at 30GHz) that they carry very little weight in the estimation of cosmological parameters and so are ignored here. The main purpose of these lower frequency channels is to monitor the free-free and synchrotron contributions from the Galaxy.

For Planck, we have adopted parameters for the four lowest frequency channels for the high-frequency instrument (HFI), as in the current design submitted to ESA (Puget *et al.* 1998). The Planck payload is in a state of active development and may change as the design of the Planck instruments is refined. However, the parameters listed in Table 2 give an accurate indication of what Planck is intended to achieve. The major difference in the current Planck payload compared to that described in the Phase A report is the addition of polarization sensitivity in the HFI instrument at 143, 217 and 545 GHz and a much improved performance of the low-frequency instrument (LFI), which covers the frequency range 31 – 100 GHz. The proposal to cool the LFI to 20K is expected to improve its sensitivity to within a factor of two (or better) of that of the HFI. The parameters listed in Table 2 for Planck are thus likely to underestimate the total sensitivity achievable by summing over all frequency channels.

Evidently, there are some uncertainties in the experimental parameters, particularly for Planck. We emphasise, therefore, that the numbers given in this paper are meant to be illustrative of the degeneracies among cosmological parameters resulting from experiments with the characteristics of MAP and Planck, rather than a precise analysis of these satellites. A detailed analysis should include systematic errors arising from Galactic and extra-Galactic foregrounds, scanning strategy and map reconstruction, and power-spectrum estimation. A considerable amount of work along these lines has been done already (*e.g.* Bouchet, Gispert and Puget 1995, Tegmark and Efstathiou 1996, Bouchet *et al.* 1997, Hobson *et al.* 1998, Delabrouille, 1998) and will be developed in the future using more precise models of the satellites. In this paper, we assume that the CMB power spectrum can be measured to the theoretical variance given by equation (5a) over half of the sky, $f_{sky} = 0.5$. We therefore ignore any non-primordial contributions to the CMB anisotropies (except in Section 5), assuming that these can be subtracted to high accuracy using the frequency information available with both satellites.

The three sets of parameters in Table 2 are also useful for presentational purposes, since they help illustrate some of the key points of this paper. The OMAP specifications are close to a threshold at which there are large degeneracies between estimates of cosmological parameters. These specifications have been retained for their pedagogical value, even though the actual MAP performance is expected to be much better. As we show in Sections 3 and 4, the CMAP parameters (primarily the higher angular resolution) lead to a significant improvement in cosmological parameter estimates. Of course, this is the main motivation for improving the angular resolution of MAP compared to the original design specification. The parameters for Planck define an experiment that is almost 'cosmic-variance limited', *i.e.* where random experimental errors are less important than the sampling errors arising from the fact that we can observe only one realisation of microwave sky. In summary, we will see in later sections that degeneracies among cosmological parameters are severe for OMAP, the results for Planck are close to the best that can be achieved from observations of the primary CMB anisotropies alone, and the results for CMAP are intermediate between these two cases.

3 GEOMETRICAL DEGENERACY

3.1 Cosmological parameters

We specify a spatially flat target cold dark matter (CDM) model defined by the following parameters:

• Spectral indices n_s and n_t for the scalar and tensor components. The target model has $n_s = 1$ and $n_t = 0$.

• The overall amplitude of the CMB anisotropy spectrum defined by the average band power $\langle \ell(\ell+1)C_\ell/(2\pi)\rangle^{1/2}$ over the range of multipoles ℓ_{max} accessible to the experiment. We denote this amplitude, relative to a COBE normalized model, by Q. The target model has $Q = 1$.

• The ratio r of the tensor and scalar components $r = C_2^t/C_2^s$. The target model has $r = 0.2$.[†]

• The cosmological densities, Ω_i, of the various constituents of the universe, relative to the critical density of the Einstein -de Sitter model. We include the contribution from baryons Ω_b, cold dark matter Ω_c, a cosmological constant $\Omega_\Lambda = \Lambda/(3H_0^2)$ (where H_0 is Hubble's constant), and a density parameter that characterises the spatial curvature of the Universe:

$$\Omega_k = 1 - \Omega_b - \Omega_c - \Omega_\Lambda \,. \tag{6}$$

The CMB anisotropies are determined directly by *physical* densities, ω_i, which are related to the density parameters Ω_i

[†] In inflationary models with an exactly uniform rate of acceleration the ratio r and the tensor and scalar spectral indices are related via $r \approx -7n_t = 7(1 - n_s)$ (see *e.g.* Davis *et al.* 1992, Liddle and Lyth 1992, Bond *et al.* 1994). The parameters of the target model are slightly inconsistent with these relations, though this is of no consequence for any of the subsequent results in this paper.

Table 1: Experimental Parameters

	OMAP			CMAP			PLANCK			
ν (GHz)	40	60	90	40	60	90	100	150	220	350
θ_{fwhm}	$32'$	$23'$	$17.4'$	$28'$	$21'$	$12.6'$	$10.7'$	$8'$	$5.5'$	$5'$
$\sigma_{pix}/10^{-6}$	7.6	10.8	16.3	6.6	12.1	25.5	1.7	2.0	4.3	14.4
$w_c^{-1}/10^{-15}$	4.9	5.4	6.8	2.9	5.4	6.8	0.028	0.022	0.047	0.44

by $\omega_i = \Omega_i h^2$, where h is Hubble's constant H_0 in units of 100 $\mathrm{kms}^{-1}\mathrm{Mpc}^{-1}$. We therefore use the physical densities ω_i to specify the target model. The Hubble constant then becomes a secondary parameter that is fixed by the constraint equation

$$h^2 = \omega_b + \omega_c + \omega_k + \omega_\Lambda \,. \tag{7}$$

The target model has $\omega_b = 0.0125$, $\omega_c = 0.2375$, $\omega_k = 0$, $\omega_\Lambda = 0$, *i.e.* $\Omega_b = 0.05$, $\Omega_c = 0.95$, $\Omega_k = 0$, $\Omega_\Lambda = 0$ and $h = 0.5$. The advantages of using the densities ω_i for parameter estimation have been discussed previously by BET97, and will become obvious in the next two sections.

The target model is therefore specified by 8 parameters, 4 parameters defining the spectrum of fluctuations (two amplitudes and two spectral indices); and 4 density parameters specifying the matter content and geometry of the universe. This is a relatively small parameter set, but has been chosen to illustrate some key points concerning parameter degeneracies. There would be little value in including, for example, additional matter components such as hot dark matter, or relativistic matter, since this would complicate the discussion of degeneracies without adding anything substantially new.

We have not included any parameters to specify reionization of the intergalactic medium, *e.g.* an optical depth to Thomson scattering, τ_{opt}. This is because in the absence of polarization measurements, the effects of reionization are almost completely degenerate with a change in the amplitude of the fluctuations (*i.e.* the product $Qe^{\tau_{opt}}$ is equal to a constant). With polarization information, it is possible to break the degeneracy between Q and τ_{opt}, provided τ_{opt} is large enough (see ZSS97). The measurement of polarization also offers a possibility of distinguishing between tensor and scalar modes (Crittenden and Turok 1995, Seljak 1997a, Kamionkowski and Kosowsky 1998). If the polarization pattern can be reliably decomposed into electric and magnetic components, it is possible to determine the relative amplitudes of the scalar and tensor modes to much higher accuracy than is possible from observations of the total CMB anisotropy alone. Such a measurement would have a large qualitative impact on the parameter estimates described in the next two sections, significantly reducing the degeneracies between the tensor parameters and other cosmological parameters. However, the tensor contribution to the polarization signal is very small and concentrated to low ℓ values, so may be difficult to measure against contaminating polarization signals of Galactic origin.

3.2 The angular diameter distance degeneracy

Two physical scales play a crucial role in determining the shape of the CMB anisotropy spectrum. These are the sound horizon $r_s(a_r)$ at the time of recombination, and the angular diameter distance d_A to the last scattering surface. (The quantity a_r is the cosmological scale factor at recombination, normalized to unity at the present epoch). The sound horizon defines the physical scales for the Doppler peak structure that depends on the physical matter densities ω_b and ω_c, but not on the value of the cosmological constant or spatial curvature since these are dynamically negligible at the time of recombination. The angular diameter distance depends on the net matter density, $\omega_m \equiv \omega_b + \omega_c$, ω_k and ω_Λ and maps the physical positions of the Doppler peaks to peaks in the angular power spectrum C_ℓ as a function of multipole ℓ. This mapping leads to a nearly exact 'geometrical' degeneracy among cosmological parameters, as has been noted by BET97 and ZSS97. Models will have almost exactly the same CMB anisotropy spectra at high multipoles if they satisfy the following criteria:
[1] they have identical matter densities ω_b and ω_c;
[2] identical primordial fluctuation spectra;
[3] identical values of the parameter[‡]

$$\mathcal{R} = \frac{\omega_m^{1/2}}{\omega_k^{1/2}} \sinh\left[\omega_k^{1/2} y\right] \tag{8a}$$

where

$$y = \int_{a_r}^{1} \frac{da}{[\omega_m a + \omega_k a^2 + \omega_\Lambda a^4 + \omega_Q a^{1-3w_Q}]^{1/2}}. \tag{8b}$$

Here ω_Q refers to a component of the energy density that obeys an equation of state with fixed pressure to density ratio, $w_Q = p/\rho$, as might arise with scalar fields which are important at late times in the universe, *e.g.*, Ratra and Peebles 1988 and Caldwell, Dave and Steinhardt 1998 (who have dubbed such phenomena quintessence). Note that $w_Q = -1/3$ gives the same contribution as ω_k gives in y, but the geometrical aspects of the ω_k angle-distance relation are absent, yielding a behaviour more similar to that of ω_Λ. Since it therefore does not add qualitatively new features

[‡] Throughout this paper we restrict our analysis to models with negative spatial curvature (positive Ω_k). There is no fundamental reason for imposing this restriction, since it is straightforward to generalize expressions such as equation (8a) to models with positive curvature. However, all of the numerical examples described in this paper have been computed with an updated version of the CMB anisotropy code of Seljak and Zaldarriaga (1996) which is restricted to models with negative spatial curvature.

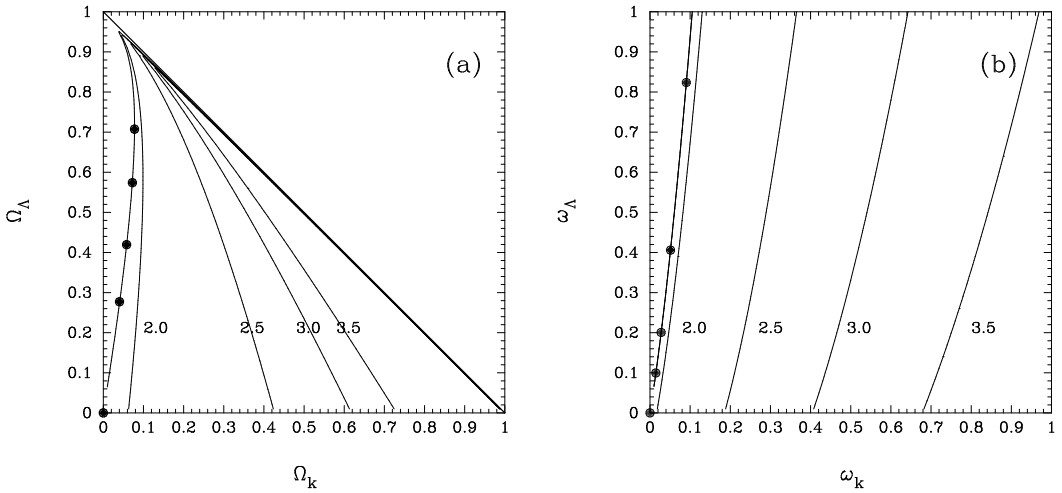

Figure 1. Figure 1a shows degeneracy lines of constant $\mathcal{R}$ in the Ω_Λ-Ω_k plane. The value of $\mathcal{R}$ is given next to each line. In computing this figure, the matter density parameter is fixed by the constraint $\Omega_m = 1 - \Omega_k - \Omega_\Lambda$. Figure 1b shows lines of constant $\mathcal{R}$ in the ω_Λ-ω_k plane for a universe with $\omega_m = 0.250$. The five dots in each figure show the locations of the five models with nearly degenerate C_ℓ spectra plotted in Figure 2. The target model with the parameters given in Section 3.1 is located at the origin in each panel.

to the discussion we ignore ω_Q terms in what follows. Equations (8a,8b) are special cases of more general expressions for the locations of the Doppler peaks given in Section 4. Provided the above conditions are satisfied, the only differences between the CMB power spectra of models with different values of Ω_Λ and Ω_k will be those at low multipoles $\ell \lesssim 30$ arising from the late-time Sachs-Wolfe effect (see Bond 1996, Hu, Sugiyama and Silk 1997, and references therein).

This is illustrated in Figures 1 and 2. Figure 1 shows lines of constant $\mathcal{R}$ in the Ω_Λ - Ω_k plane (Figure 1a) and in the ω_Λ - ω_k plane (Figure 1b), for a fixed value of $\omega_m = 0.25$. Figure 1a is the more useful, because the degeneracy lines are fixed by the two parameters Ω_Λ and Ω_k, with the matter density specified by the constraint $\Omega_m = 1 - \Omega_k - \Omega_\Lambda$. The degeneracy lines in the space defined by the physical densities ω_m, ω_k and ω_Λ require specification of all three densities or, alternatively, two densities and a value of the Hubble constant (see equation 7). We have therefore assumed the value of ω_m of our target model in computing Figure 1b.

The five dots in each panel of Figure 1 show the locations of models with nearly degenerate C_ℓ spectra. These models have the same matter densities as the target model, $\omega_b = 0.0125$ and $\omega_c = 0.2375$, and identical scalar spectral index $n_s = 1$ (we compute only the scalar component for this comparison). The five models have different values of ω_k and ω_Λ chosen to lie along the degeneracy line of $\mathcal{R} = 1.94$ of the target model, as shown in the figures. The resulting CMB power spectra are plotted in Figure 2.

As expected, the power spectra plotted in Figure 2 are indistinguishable except at small multipoles, $\ell \lesssim 30$. The lower panel compares the residuals $\Delta C_\ell / C_\ell$ for these models compared to the spatially flat target model. The two unlabelled dashed lines show the error on the residuals arising from cosmic variance alone, $\Delta C_\ell / C_\ell = \pm(2/(2\ell+1))^{1/2}$. There are several points worth noting from this figure:

[1] The differences between the models at high multipoles ($\ell \gtrsim 200$) are small and arise from numerical errors. These include small errors in the computation of the degeneracy parameter $\mathcal{R}$, but arise predominantly from numerical errors in the CMBFAST code.

[2] Although the numerical errors at high multipoles are much smaller than the cosmic variance errors, they accumulate in the computation of the Fisher matrix (equation 4) and can erroneously break the geometrical degeneracy. Thus, numerical errors in what should be an exact degeneracy can lead to extremely misleading results, in which the errors in the density parameters ω_Λ and ω_k appear weakly correlated and extremely small. This problem is particularly acute for a Planck-type experiment in which the C_ℓ estimates are nearly cosmic variance limited to high multipoles.

[3] The differences in the power spectra at low multipoles, $\ell \lesssim 30$, arise from a real physical effect – the late time Sachs-Wolfe effect – and are not caused by numerical errors. However, the differences are smaller than the cosmic variance limits and so it is impossible to differentiate between these models at a high significance level from measurements of the CMB anisotropies alone. (This point is quantified in detail in Figure 3 below).

[4] The power spectra for the low density cosmological models assume a particular model of the origin of the primordial fluctuation spectrum (in this case, power-law fluctuations in the potentials Φ and Ψ). If we were to allow complete freedom to adjust the shape of the power spectrum on large spatial scales, then we could compensate for the differences caused by the late-time Sachs Wolfe effect. The existence of the late-time Sachs-Wolfe effect cannot be used to distinguish between different cosmological models unless specific assumptions are made concerning the shape of the fluctuation spectrum.

The futility of breaking the geometrical degeneracy from linear CMB anisotropies is illustrated in Figure 3. In this figure, we have computed a grid of scalar C_ℓ spectra varying the parameters ω_Λ and ω_k, whilst fixing the remaining parameters, ω_b, ω_c and n_s to those of the spatially flat

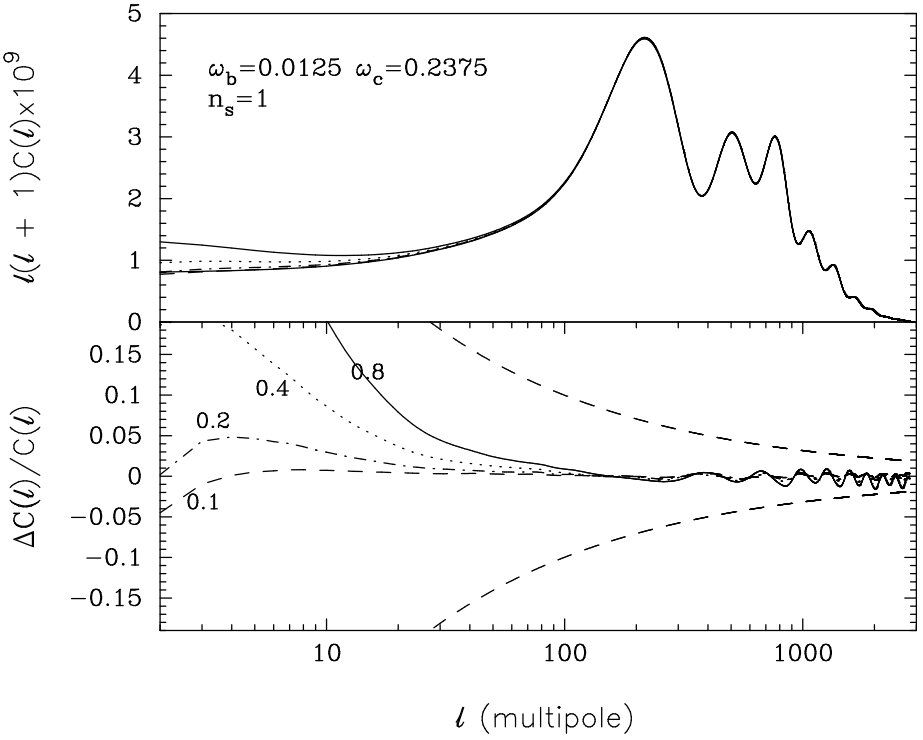

Figure 2. The upper panel shows the scalar power spectrum for the nearly degenerate models shown by the dots in Figures 1. The target model has $\omega_\Lambda = \omega_k = 0$, $\omega_b = 0.0125$ and $\omega_c = 0.2375$ and $n_s = 1$. The lower panel shows the residuals of these open universe models with respect to the spatially flat target model. The numbers next to each curve give the value of ω_Λ for each model. The two lines with long dashes show the standard deviation of the residuals from cosmic variance alone.

target model. Figure 3 shows the exact likelihood ratio,

$$-2\ln\left(\frac{\mathcal{L}}{\mathcal{L}_{max}}\right) = \sum_{\ell\le\ell_{max}} \frac{(C_\ell(\mathbf{s}) - C_\ell(\mathbf{s}_0))^2}{(\Delta C_\ell)^2}, \qquad (9)$$

for an experiment with the OMAP parameters listed in Table 2 and ℓ_{max} set to 1000. The contours show approximate 1, 2 and 3σ contours in the ω_Λ and ω_k plane assuming all other parameters are known (*i.e.* we show contours where $-2\ln(\mathcal{L}/\mathcal{L}_{max})$ equals 2.3, 6.2 and 11.8 corresponding to 68%, 95% and 99.7% confidence regions if $-2\ln(\mathcal{L}/\mathcal{L}_{max})$ is χ^2 distributed with two degrees of freedom). The 1σ contours are broken up artificially by the discrete size of the grid over which the C_ℓ's were computed numerically. The 2σ contour limits ω_Λ to be less than about 0.7 and ω_k to be less that about 0.1. The contours follow the line of constant $\mathcal{R}$ computed in Figure 1b and show that measurements of the CMB anisotropies alone cannot remove the geometrical degeneracy between ω_Λ and ω_k. Improving the accuracy of the CMB measurements simply causes the likelihood contours to narrow around the degeneracy lines. Although this has important consequences for the estimation of other cosmological parameters, improving the accuracy of the experiment does not help to remove the geometrical degeneracy. For all practical purposes, the geometrical degeneracy in linear theory is exact and can be removed only by invoking other constraints on the geometry of the Universe (*e.g.* as derived from Type Ia supernovae, Perlmutter *et al.* 1997, 1998, see Section 6), or from the effects of gravitational lensing on the CMB (Stompor and Efstathiou 1998, Metcalf and Silk 1998).

3.3 Parameter estimation including spatial curvature

In this Section, we describe how the Fisher matrix formalism can be adapted to handle the geometrical degeneracy. This can be achieved by redefining the variables $\mathbf{s}$ so that one of the derivatives $\partial C_\ell/\partial s_i$ is computed along the direction of the degeneracy (*i.e.* along lines of constant $\mathcal{R}$, as in the examples plotted in Figure 2). The derivative of C_ℓ along the degeneracy line can then be set to zero at high multipoles by construction, eliminating the effects of numerical errors in computing the elements of the Fisher matrix. This technique has been used previously by us in BET97, and gives extremely stable results.

To illustrate the method, we analyse the errors in the cosmological parameters for small variations around the target model defined in Section 3.1. The target model has $\Omega_k = 0$, $\Omega_\Lambda = 0$ and $\Omega_m = 1$, and so the derivatives of $\mathcal{R}$ are

$$\left(\frac{\partial\mathcal{R}}{\partial\Omega_k}\right)_t = 1\,, \quad \left(\frac{\partial\mathcal{R}}{\partial\Omega_\Lambda}\right)_t = -\frac{1}{7} \qquad (10a)$$

where the subscript t denotes that the derivatives are com-

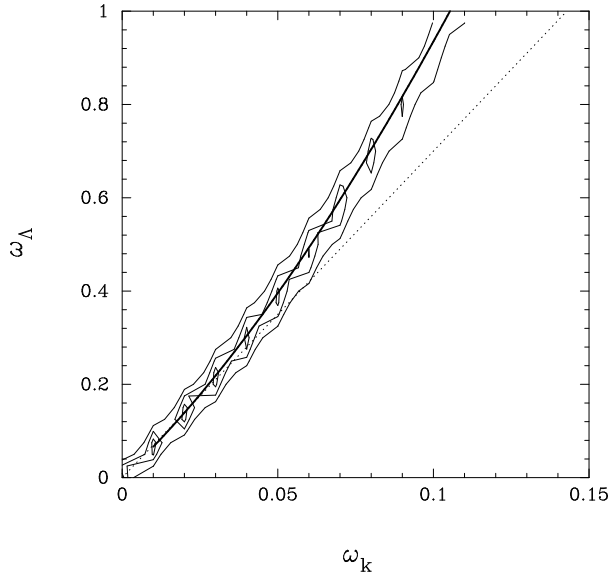

Figure 3. Likelihood ratio contours in the ω_Λ-ω_k plane for models containing only scalar modes. The models have fixed values of $\omega_b = 0.0125$ and $\omega_c = 0.2375$. The likelihood ratio for each model has been computed assuming the experimental parameters of OMAP (Table 2) and our standard spatially flat target model. The contours show where $-2\ln(\mathcal{L}/\mathcal{L}_{max})$ has values of 2.3, 6.2 and 11.8 corresponding approximately to 1σ, 2σ and 3σ contours assuming all other parameters are known. The full line shows the degeneracy curve with the same value of $\mathcal{R}$ as the target model (*cf* Figure 1b) and the dashed line shows the Taylor series approximation to this curve, $\omega_\Lambda = 7\omega_k$ (see Section 3.3).

puted at the parameter values of the target model. For small variations around the target model, the degeneracy lines in $\mathcal{R}$ follow

$$\delta\Omega_k = \frac{1}{7}\delta\Omega_\Lambda, \qquad \delta\omega_k = \frac{1}{7}\delta\omega_\Lambda. \tag{10b}$$

It is therefore useful to define an auxiliary density

$$\omega_D = 7\omega_k - \omega_\Lambda \tag{11}$$

to replace ω_k in the Fisher matrix analysis (where the subscript, D, denotes 'degeneracy') . For small variations around the target model, the constraint $\omega_D = 0$ defines the degeneracy line $\mathcal{R} =$ constant. The CMB spectra plotted in Figure 2 all have $\omega_D \approx 0$ and identical values of ω_b and ω_c. They can therefore be used to define the derivative $\partial C_\ell/\partial\omega_\Lambda$, which can be set to zero at, for example, $\ell \gtrsim 200$ to suppress the effects of numerical errors. The results of such an analysis for the experiments summarized in Table 2 are listed in Table 3.3.

The results from Table 3.3 show that the 1σ errors in ω_Λ are close to unity and extremely insensitive to the experimental details. This is in agreement with the likelihood analysis of Figure 3. The large error in ω_Λ thus reflects the geometrical degeneracy. In contrast, the error on the auxiliary density parameter ω_D decreases from 0.17 for the OMAP experimental parameters, to 0.014 for the Planck parameters. The error in ω_D is set by the accuracy to which the parameter $\mathcal{R}$ can be determined by the experiment, *i.e.* by the ability of the experiment to fix the positions of the Doppler peaks. An experiment such as Planck samples the

Table 2: 1σ **errors on estimates of cosmological parameters**

Parameter	OMAP	CMAP	PLANCK
$\delta\omega_b/\omega_b$	0.075	0.042	0.0064
$\delta\omega_c/\omega_c$	0.24	0.13	0.020
$\delta\omega_D$	0.17	0.097	0.014
$\delta\omega_\Lambda$	1.23	1.20	1.09
δQ	0.013	0.0041	0.0013
δr	0.41	0.27	0.15
δn_s	0.059	0.034	0.0065
δn_t	1.015	0.998	0.911

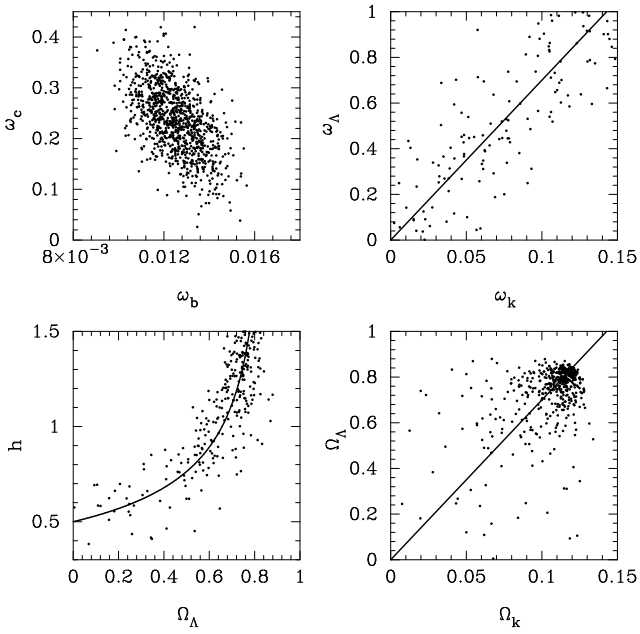

Figure 4. Results of Monte-Carlo simulations of parameter estimation as described in the text assuming the parameters of OMAP as given in Table 2. The panels show correlations between various pairs of parameters. The lines in the ω_Λ-ω_k and Ω_Λ-Ω_k plane show the degeneracy lines given by equation (10b). The line in the h-Ω_Λ plane shows the degeneracy line given by equation (12).

entire Doppler peak structure of C_ℓ and so can determine $\mathcal{R}$ (and hence ω_D) to extremely high accuracy.

Another important consequence of the geometrical degeneracy is that it sets a fundamental limitation on a determination of the Hubble constant from measurements of the primary CMB anisotropies alone. This arises because the Hubble constant is a secondary parameter, determined from the constraint equation (7). The error in the determination of h will be dominated by the error in ω_Λ, which, as we have seen above, is essentially unconstrained because of the geometrical degeneracy. The value of h determined from the CMB anisotropies is therefore degenerate with the value of Ω_Λ. For satellite experiments such as MAP and Planck, we can assume to a good approximation that the parameters ω_b, ω_c and ω_D are determined exactly. Equation (7) then

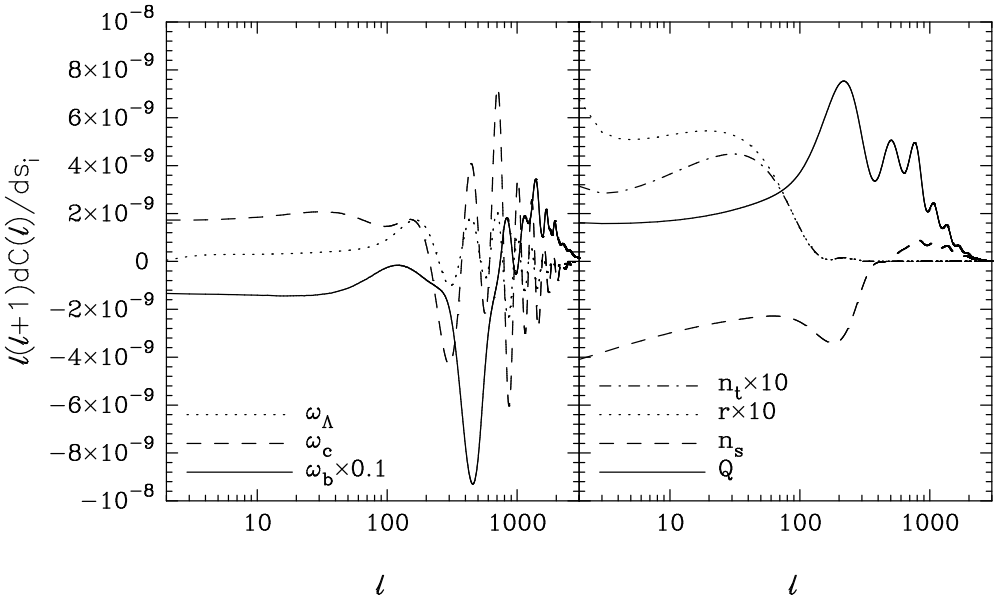

Figure 5. Derivatives of C_ℓ with respect to the seven parameters of the spatially flat target model defined in the text. The derivatives with respect to ω_b, n_t and r have been multiplied by the factor indicated in the figure (*e.g.* the derivative $\partial C_\ell/\partial\omega_b$ has been divided by a factor of ten).

provides a relation between h and Ω_Λ

$$h = h_t/(1-\frac{8}{7}\Omega_\Lambda)^{1/2}\,. \tag{12}$$

Here, h_t denotes the Hubble constant of the target model. Formally, equation (12) is valid for small variations around the target model parameters, but in practice it is reasonably accurate for large variations in Ω_Λ (because the degeneracy lines in Figure 1b are very nearly straight lines). Equation (12) is independent of the details of the experiment. The scatter around the relationship (12), however, is set by the errors of the density parameters (mainly errors in ω_D) and so depends on the experimental parameters.

These points are illustrated in Figure 4 which shows the results of parameter estimation applied to a set of simulated C_ℓ spectra. Here we have generated C_ℓ spectra of our target model with errors computed for the OMAP experiment and we have determined the cosmological parameters for each model by χ^2 minimisation, assuming that the theoretical spectra of neighbouring points can be approximated by the Taylor series expansion

$$C_\ell(\mathbf{s}_i) = C_\ell(\mathbf{s}_0) + \left(\frac{\partial C_\ell}{\partial s_i}\right)\cdot\Delta s_i. \tag{13}$$

This procedure is designed by construction to mimic the Fisher matrix approach exactly. Figure 4 shows that ω_c and ω_b are slightly anticorrelated, with errors as given in Table 3.3. The parameters ω_Λ and ω_k are extremely highly correlated along the degeneracy line defined by equation (10b). The scatter about this line is determined by the errors in ω_D. The parameters h and Ω_Λ are also strongly correlated, following equation (12) to high accuracy. The final plot in Figure 4 shows the parameters Ω_Λ plotted against Ω_k. This plot may seem a little strange, because it shows a clump of points at $\Omega_\Lambda\sim0.8$ and $\Omega_k\sim0.13$, well away from the target model parameters $\Omega_\Lambda=\Omega_k=0$. This is because the errors in ω_Λ and ω_D are symmetrical by construction and we determine Ω_Λ and Ω_k from ω_Λ, ω_D and the Hubble constant as computed from the constraint relation of equation (7). Since the error in ω_Λ is large, the points in the Ω_Λ–Ω_k plane must, by construction, cluster around the values $\Omega_\Lambda\approx7/8$, $\Omega_k\approx1/8$.

In summary, the geometrical degeneracy leads to a fundamental indeterminacy in the parameters Ω_Λ and Ω_k. For spatially flat target models, this leads to a near indeterminacy of Ω_Λ and an error on Ω_k of ~0.1 irrespective of the accuracy of the CMB experiment. The indeterminacy of Ω_Λ leads to an indeterminacy of the Hubble constant via the constraint relation (7). As a corollary, independent constraints on H_0 and Ω_Λ from observations other than the CMB anisotropies can be used to break the geometrical degeneracy.

The discussion of this Section also shows that tables designed to demonstrate the power of various experiments, such as Table 3.3, must be interpreted with caution. Evidently the errors on some cosmological parameters are extremely sensitive to the assumed parameter set. For example, restricting to models with zero cosmological constant, or curvature, would have a very large effect on the accuracy of the determination of H_0. Similar remarks apply to other parameters and to near degeneracies other than the geometrical degeneracy described here. This is the topic of the next Section.

4 EIGENVECTORS OF THE FISHER MATRIX AND PARAMETER DEGENERACIES

4.1 Motivation

The geometrical degeneracy described in the previous Section represents an extreme case of a near exact degeneracy between cosmological parameters. In this Section, we will investigate partial degeneracies among other parameters showing, for example, how uncertainties in the parameters defining the primordial spectra couple to the cosmological densities in baryons and CDM. The results of the previous section show that the geometrical degeneracy is so nearly exact that very little is lost in analysing degeneracies among other parameters by restricting to a spatially flat background universe. Such a restriction merely removes the geometrical degeneracy from consideration without affecting any other aspect of the analysis. In this Section, we therefore analyse the parameter errors for the same spatially flat target model as defined in Section 3.1 but restricted to a set of 7 parameters, n_s, n_t, Q, r, ω_b, ω_c and ω_Λ. The derivatives of C_ℓ with respect to these seven parameters are plotted in Figure 5.

4.2 Principal components

The Fisher matrix F is a symmetric $n \times n$ matrix and so can be reduced to diagonal form,

$$F = U\Lambda U^\dagger, \qquad \Lambda = \mathrm{diag}(\lambda_1, \lambda_2, ..., \lambda_n)\,, \tag{14}$$

where U is the matrix in which the m'th row is the eigenvector $\mathbf{u}_m$ corresponding to the eigenvalue λ_m. The eigenvectors are assumed ordered so that $\lambda_1 \geq \lambda_2 \geq \lambda_3 ... \geq \lambda_m$. From our original variables $\mathbf{s}$ we can therefore construct a set of new variables $\mathbf{X}$ that are orthogonal to each other,

$$\mathbf{X} = U^\dagger \mathbf{s}, \qquad \mathbf{s}^\dagger F \mathbf{s} = \mathbf{X}^\dagger \Lambda \mathbf{X}. \tag{15}$$

Thus, for a given experiment and set of parameters s_i, we can construct a set of variables X_i that are orthogonal linear combinations of the original variables; X_1 is the most accurately determined parameter, X_2 is the next most accurately determined parameter and so on. We call the variables $\mathbf{X}$ the principal components of the experiment, and refer to X_7, X_6 *etc* as 'low-order' components because they are poorly constrained (smallest eigenvalues) and X_1, X_2, *etc* as 'high-order' components.

We have computed the eigenvalues and principal components for each set of experimental parameters listed in Table 2. The results are given in Table 4.1, which lists the components of the projection vector $U^\dagger$ relating the principal components to the original variables s_i. (Note that the numbers in Table 4.1 are computed assuming that the variables s_i have zero mean.) The derivatives of C_ℓ with respect to the principal components for each experiment are plotted in Figure 6. We make the following points concerning this analysis:

[1] As in many aspects of multivariate analysis, certain results depend on the scaling of the parameters. The principal components in Table 4.1 are not unique and depend on the relative scalings of the variables s_i, as well as on the functional form of the variables (*e.g.* whether we use $\log \omega_b$ instead of ω_b, or Q^2 instead of Q). One must therefore be cautious in assigning a physical interpretation to the principal components. The point of view adopted here (in line with most applications of principal component analysis, see *e.g.* Kendall 1975) is that the principal components provide a computational tool for assessing whether a set of observational points $\mathbf{s_i}$ lie within a sub-space of the n-dimensional hyperspace, $i = 1, \ldots n$. (*i.e.* whether there are degeneracies among the physical parameters which are unresolved by the experiment).

[2] The standard deviation of the principal component X_i is equal to $\lambda_i^{-1/2}$. Thus, the eigenvalues have sometimes been used to indicate the power of a CMB experiment (*e.g.* BET97). For example, from Table 4.1 we see that OMAP determines three principal components to an accuracy of $\leq 10^{-3}$, while CMAP and Planck determine 4 and 5 components respectively to this accuracy or better. While this is true, what is important is how many *physical* (*i.e.* cosmologically interesting) parameters can be determined to high accuracy rather than the number of linear combinations like principal components that can be determined to high accuracy.

[3] The derivatives of C_ℓ with respect to the physical variables plotted in Figure 5 can be broadly grouped into two categories: those that depend on inflationary variables, n_s, n_t and r that are largest at low multipoles, and those that depend on physical densities, ω_b, ω_c, ω_Λ, that have significant amplitudes to $\ell \sim 2000$—3000. Cosmic variance sets a fundamental limit to the accuracy with which the variables n_s, n_t and r can determined from observations of the CMB, whereas the cosmic densities can be determined to high precision if C_ℓ is measured accurately at high multipoles. Thus, the power of an experiment can be gauged by the extent to which the principal components (particularly those with the largest variances) mix inflationary variables with cosmic densities. Qualitatively, this can be assessed from Figure 6. For OMAP and CMAP, the C_ℓ derivatives with respect to the low-order principal components are oscillatory and have a significant amplitude at multipoles $\ell \sim 100$ – 2000. This tells us immediately that the low-order principal components involve the cosmic densities at some level and hence that they will be partially degenerate with inflationary variables, which is obviously unsatisfactory if we want to measure the cosmic densities to high accuracy.

[4] The principal components for a Planck-type experiment are nearly equivalent to physical variables. In Table 4.1, we have placed an asterisk next to each entry with an absolute value greater than 0.5, so that the reader can see easily which physical variables contribute strongly to each principal component. For Planck, X_1, X_2, X_3, X_4 and X_5 couple strongly to ω_b, ω_c, Q, n_s and ω_Λ respectively. The two lowest order principal components are made up predominantly of the two tensor parameters r and n_t. Nevertheless, the degeneracies that remain dominate the errors of the cosmological densities. These remaining degeneracies are, in a sense, fundamental, because they cannot be removed by making more accurate observations of the linear CMB temperature anisotropies. The results for Planck shown in Table 4.1 and Figure 6 are very close to those for an experiment limited by cosmic variance alone. Accurate CMB *polarization* measurements on large scales could, however, constrain the tensor component and so improve the accuracies of the cosmic densities. Section 4.6 demonstrates how the accuracies of the cosmic densities ω_b and ω_c are affected by constraints on the tensor component.

In the rest of this Section, we investigate the degen-

Table 3: Principal components

OMAP errors

$1/\sqrt{\lambda}$	ω_b	ω_c	ω_Λ	Q	n_s	r	n_t
2.27E-4	0.998*	-1.417E-2	-1.103E-2	-6.376E-2	4.919E-3	-2.972E-4	-2.599E-4
3.14E-3	5.363E-2	-0.284	3.051E-3	0.871*	-0.397	1.258E-2	1.188E-3
4.46E-3	2.727E-2	0.886*	0.321	1.513E-2	-0.294	2.910E-2	2.633E-2
1.91E-2	2.722E-2	0.135	0.214	0.424	0.829*	-0.198	-0.167
4.32E-2	-6.283E-3	-0.312	0.821*	-0.183	-0.191	0.300	-0.261
3.18E-1	3.315E-3	-0.134	0.416	1.798E-2	0.177	0.565*	0.676*
1.06	6.271E-4	-1.768E-2	5.901E-2	4.918E-3	2.753E-2	0.742*	-0.667*

CMAP errors

$1/\sqrt{\lambda}$	ω_b	ω_c	ω_Λ	Q	n_s	r	n_t
1.89E-4	0.998*	-1.592E-2	-1.113E-2	-6.241E-2	3.257E-3	-2.052E-4	-1.795E-4
2.98E-3	4.883E-2	-0.366	-3.678E-2	0.862*	-0.344	1.005E-2	9.545E-3
3.82E-3	3.571E-2	0.870*	0.314	0.279	-0.252	2.238E-2	2.0370E-2
1.22E-2	2.471E-2	0.149	-6.142E-2	0.415	0.886*	-9.596E-2	-8.279E-2
3.39E-2	2.270E-3	-0.261	0.849*	-4.378E-2	5.800E-2	-0.345	-0.295
2.46E-1	3.025E-3	-0.136	0.417	1.385E-2	0.171	0.616*	0.631*
0.997	-2.923E-4	1.032E-2	-3.328E-2	-1.769E-3	-1.260E-2	-0.701*	0.712*

PLANCK errors

$1/\sqrt{\lambda}$	ω_b	ω_c	ω_Λ	Q	n_s	r	n_t
4.09E-5	0.999*	-3.110E-2	-1.707E-2	3.253E-2	1.847E-2	-1.088E-5	-9.348E-6
5.29E-4	3.195E-2	0.958*	0.274	6.588E-2	2.740E-2	2.852E-4	2.541E-4
7.42E-4	-3.704E-2	-5.976E-2	-4.110E-2	0.977*	0.196	8.106E-4	7.508E-4
4.32E-3	-1.172E-2	-3.611E-2	7.679E-2	-0.195	0.976*	-3.396-2	-3.025E-2
5.25E-2	7.997E-3	-0.275	0.957*	3.922E-2	-7.733E-2	3.716E-3	3.843E-3
5.54E-2	-5.331E-4	-4.795E-4	-2.665E-3	-1.017E-2	4.461E-2	0.760*	0.648*
0.75	-1.424E-5	1.003E-4	-4.164E-4	-2.579E-4	9.970E-4	-0.649*	0.761*

Table 1. Components of the projection vector $U^\dagger$ relating the original variables $\hat{s}_i$ (with means subtracted, $\hat{s}_i = s_i - \langle s_i \rangle$) to the principal components $\mathbf{X}$. The eigenvalues are listed in the first column. We have marked each component of $U^\dagger$ that is greater than 0.5 with an asterisk to show which physical variables contribute significantly to each principal component.

eracies among cosmological parameters as defined by the low-order principal components. We conclude this Section by listing in Table 4.2, under the column headings 'all pc', the 1σ errors in the cosmological parameters derived from the Fisher matrix for the spatially flat case.

For most of the parameters, the error estimates are close to those listed in Table 3.3. The errors on ω_Λ in Table 4.2 are obviously much smaller than those given in Table 3.3 because we are restricting to a spatially flat background model. The errors on ω_Λ will be discussed in greater detail in Section 4.4. The largest differences between Tables 3.3 and 4.2 are for the errors in the tensor parameters r and n_t. The errors on these parameters are very large, so the first order expansion of C_ℓ, on which the Fisher matrix expression (4) is based, cannot necessarily be expected to give accurate answers.

4.3 Degeneracies among cosmic parameters

The columns in Table 4.2 labelled '1pc', '2pc' and '3pc', list the variances of the cosmological parameters that arise if we include in the Fisher matrix analysis only the lowest order principal component (X_7, column labelled '1pc'), the two and three lowest order principal components (X_6 and X_7 in the column labelled '2pc', and X_5, X_6 and X_7 in the column labelled '3pc'). *For CMAP and OMAP, the two lowest order principal components account for most of the variance of all the cosmological parameters listed in the table.* Since we have specialized to a spatially flat universe, the geometrical degeneracy described in Section 3 has been explicitly removed from the analysis. Nevertheless, to a good approximation, the parameters of Table 4.2 lie on a two dimensional surface within the 7-dimensional parameter space. It is the orientation of this surface with respect to the axes defined by the parameters that accounts for the most of their variance.

This is illustrated in Figure 7. In Figure 7a, we have generated points in the 7-dimensional space of our cosmological

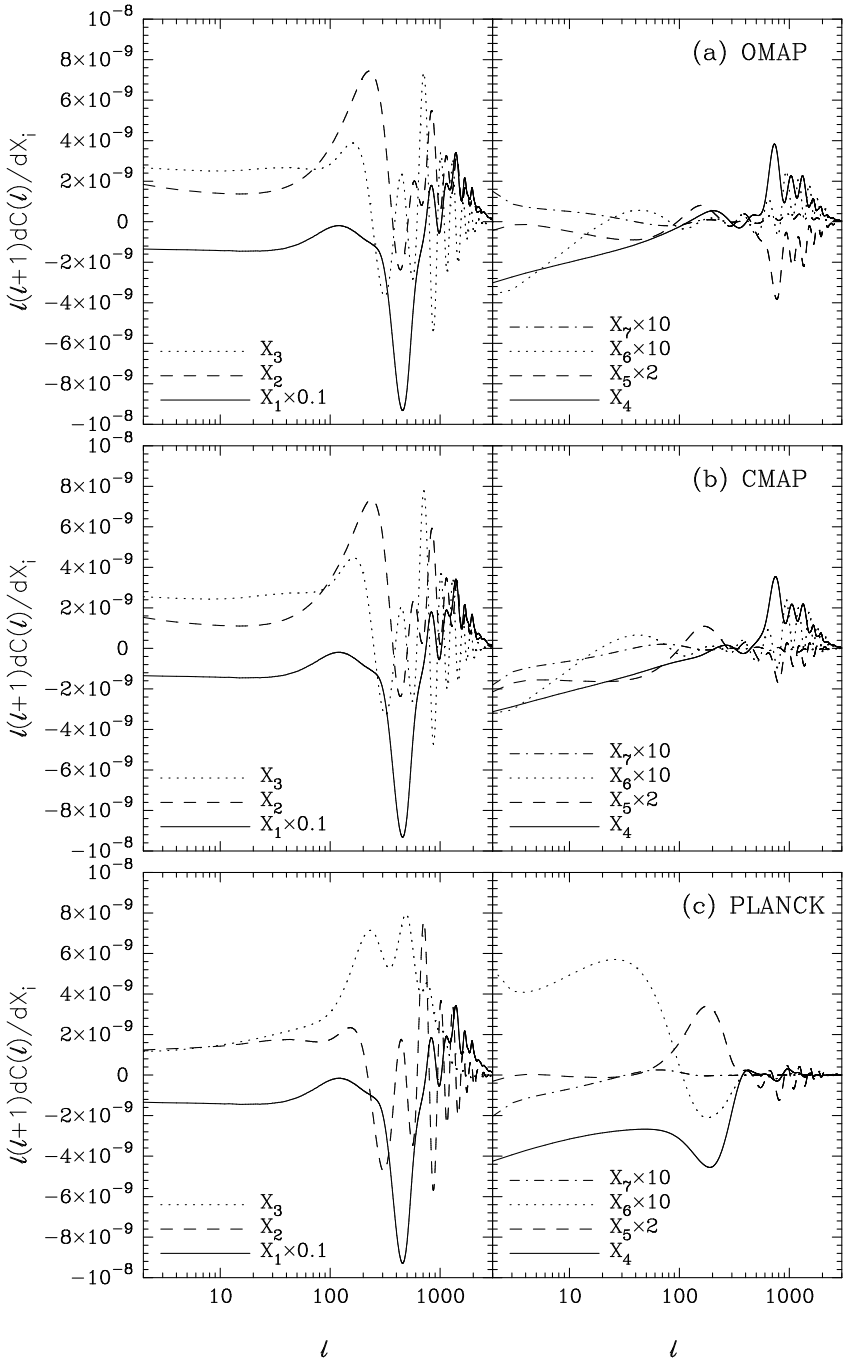

Figure 6. Derivatives of C_ℓ with respect to the principal components listed in Table 4.1 for the OMAP, CMAP and Planck experiments. The principal components have been ordered so that X_1 is the most accurately determined (*i.e.* has the largest eigenvalue), X_2 is the next most accurately determined and so on. The derivatives of C_ℓ with respect to X_1 and X_5–X_7 have been multiplied by the factors indicated in each figure.

parameters by using all principal components as given in Table 4.1 for the OMAP experiment. The principal components are assumed to be Gaussian distributed with dispersion equal to $1/\sqrt{\lambda_i}$. We have made one significant change to the Fisher matrix analysis of Section 2 in that we have applied a constraint that the densities ω_i and amplitude r must be positive. This is evidently physically reasonable for the ω_i, required for r, and aids in the comparison with the exact calculations shown in Figure 7c, to be described below.

We show correlations between various pairs of parameters, but note in particular the very strong correlations between ω_Λ and ω_c and between h and Ω_Λ. The points in these plots lie tightly on lines, similar to the situation shown in Figure 4, which illustrated the geometrical degeneracy. As we will show below, the strong correlations between ω_Λ and ω_c and h and Ω_k have a similar physical explanation to the geometrical degeneracy, though the degeneracy is not exact in this case.

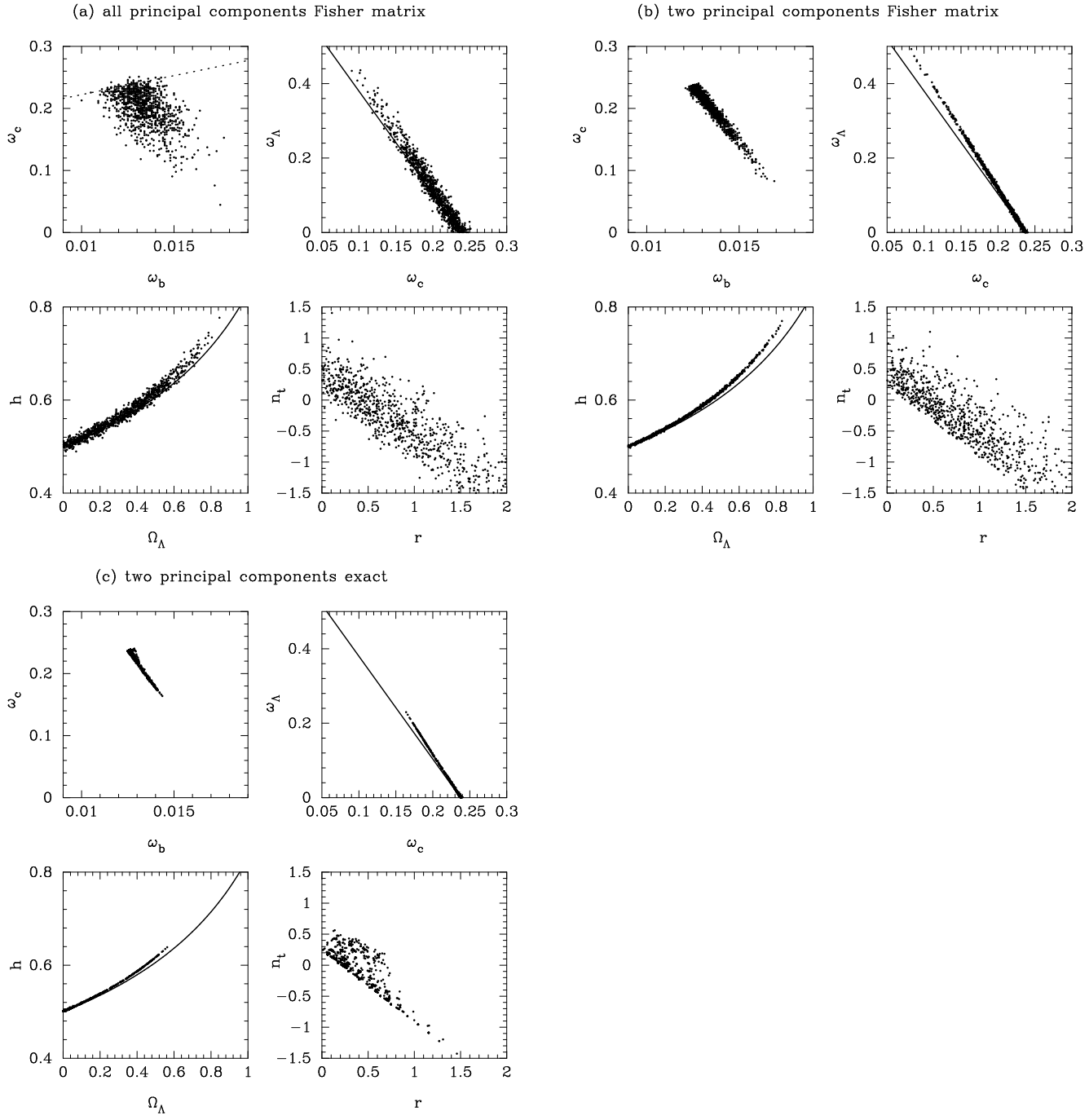

Figure 7. Monte-Carlo simulations of parameter estimation as described in the text showing correlations between various pairs of parameters. We assume the experimental parameters for OMAP as given in Table 2. In panel (a) we generate simulations using all principal components, reproducing the variances and correlations computed from the Fisher matrix. In panel (b) we generate simulations using only the two lowest order principal components X_6 and X_7 (Table 3.3). In panel (c) we show the results of an exact likelihood analysis applied to a two-dimensional grid of models in the variables X_6 and X_7 (see Figure 8 and the discussion in the text). The solid lines in the ω_Λ—ω_c and h—Ω_Λ panels are computed from equations (23a) and (23b). The dashed line in the ω_c–ω_b plane shows the degeneracy line given by a constant height for the first Doppler peak as described in Section 4.5.

Table 4: 1σ errors in estimates of cosmological parameters (spatially flat universe)

		OMAP		
Parameter	all pc	1pc	2pc	3pc
$\delta\omega_b/\omega_b$	0.11	0.056	0.098	0.10
$\delta\omega_c/\omega_c$	0.21	0.080	0.19	0.20
$\delta\omega_\Lambda$	0.15	0.064	0.14	0.15
δQ	0.014	0.0052	0.0079	0.011
δr	0.81	0.81	0.81	0.81
δn_s	0.066	0.030	0.062	0.063
δn_t	0.745	0.73	0.74	0.74
		CMAP		
Parameter	all pc	1pc	2pc	3pc
$\delta\omega_b/\omega_b$	0.072	0.024	0.063	0.064
$\delta\omega_c/\omega_c$	0.15	0.044	0.15	0.15
$\delta\omega_\Lambda$	0.11	0.034	0.11	0.11
δQ	0.0071	0.0018	0.0038	0.0041
δr	0.70	0.70	0.70	0.70
δn_s	0.046	0.0013	0.044	0.044
δn_t	0.71	0.71	0.71	0.71
		PLANCK		
Parameter	all pc	1pc	2pc	3pc
$\delta\omega_b/\omega_b$	0.0068	0.0008	0.0024	0.0040
$\delta\omega_c/\omega_c$	0.0063	0.0003	0.0003	0.0060
$\delta\omega_\Lambda$	0.0049	0.0003	0.0003	0.0049
δQ	0.0013	0.0002	0.0006	0.0006
δr	0.49	0.49	0.49	0.49
δn_s	0.0050	0.0008	0.0026	0.0026
δn_t	0.57	0.57	0.57	0.57

Figure 7b is constructed in exactly the same way as Figure 7a, except that we include only the two lowest order principal components. As expected from the entries in Table 4.2, by incorporating only the two lowest order principal components, we reproduce the degeneracy lines in Figure 7a which account for most of the variance of the physical parameters. The higher order principal components contribute to the scatter around these degeneracy lines but do not contribute much to the total variance.

Table 4.2 shows that the errors on some physical variables are large (*e.g.* ω_Λ, r, n_t). As a consequence, the variances of the low order principal components are also large and so this raises a question concerning the validity of the Fisher matrix approach to parameter errors, since this relies on small variations Δs_i of the parameters around those of the target model. To test the validity of the Fisher matrix approach, we have computed an exact version of Figure 7b using maximum likelihood. We define a 400×400 grid in the principal components X_6 and X_7 and compute scalar and tensor power spectra using the CMBFAST code. The ranges of X_6 and X_7 are illustrated in Figure 8a. The contours in Figure 8a show 1, 2 and 3σ contours for the likelihood ratio computed from equation (9) with $\ell_{max} = 1000$. The jagged lower boundary of the contours in the figures is imposed by positivity constraints on the physical parameters, *i.e.* we cannot allow negative values of ω_b, ω_c and r and (in this example) we do not allow negative values of ω_Λ. The cross in Figure 8a shows the $\pm1\sigma$ errors on X_6 and X_7 computed from the eigenvalues listed in Table 4.1; note that the scales of X_6 and X_7 in this figure have been chosen so that the error contours computed from the Fisher matrix are circular. Qualitatively, the likelihood errors are of about the same size as those computed from the eigenvalues, but the distributions computed from the likelihood function are more sharply peaked than a bivariate Gaussian distribution. This, together with the positivity constraints which further narrows the distribution, means that the errors in X_6 and X_7 computed from the likelihood ratios are smaller than those computed from the eigenvalues of the Fisher matrix.

Figure 8b shows a series of Monte-Carlo simulations. For each point plotted in the figure we generated a simulated power spectrum C_ℓ assuming Gaussian errors with variance given by equation (5a) with the parameters of the OMAP experiment listed in Table 3.3. For each simulated C_ℓ spectrum, we computed the maximum likelihood values of X_6 and X_7 by comparing with the grid of numerical models computed with CMBFAST. (In fact, we reduce the effect of the finite grid using bi-linear interpolation to compute the maximum likelihood values of X_6 and X_7.) Each point in Figure 8b is plotted at the best fitting value of X_6 and X_7, and the distribution of points follows the likelihood contours extremely well showing that our computations are self consistent. From the values of X_6 and X_7, we compute the physical parameters s_i and so we can plot an analogue of Figure 7b using parameters computed from an exact likelihood approach. This is shown in Figure 7c. The general trends between the variables are similar to those shown in Figures 7a and 7b, but the ranges are significantly narrower showing that the Fisher matrix approach overestimates the errors of the physical parameters. The Fisher matrix approach does give qualitatively correct results (which is impressive given the large errors in some of the physical variables) but evidently does not give precise error estimates.

Furthermore, since much of the variance in all of the physical parameters comes from variations of the two lowest order principal components, the Fisher matrix approach *will overestimate the errors in apparently well determined parameters such as* ω_b, since these are dominated by the variances of the low-order principal components. This is also illustrated by the entries in Table 4.3 which is a tabular version of Figure 7. The second and third columns list the variances of the physical parameters (including h and Ω_Λ) computed from all principal components and the two lowest order principal components; these numbers differ from the corresponding numbers for OMAP in Table 4.2, only because we have applied positivity constraints on r and the densities ω_Λ, ω_c and ω_b. The fourth column shows the 1σ errors in the physical parameters computed from the Monte-Carlo simulations plotted in Figure 7c. Table 4.3 shows that the Fisher matrix overestimates the errors in many of these parameters by a factor of two or so.

The example shown in Figure 7c and Table 4.3 shows how the principal component analysis can be used to simplify a likelihood calculation of the errors in cosmological parameters, so improving on the Fisher matrix approximation. In general, the cosmological parameters defining a model $\mathbf{s}_i$ are highly degenerate with respect to each other and so the

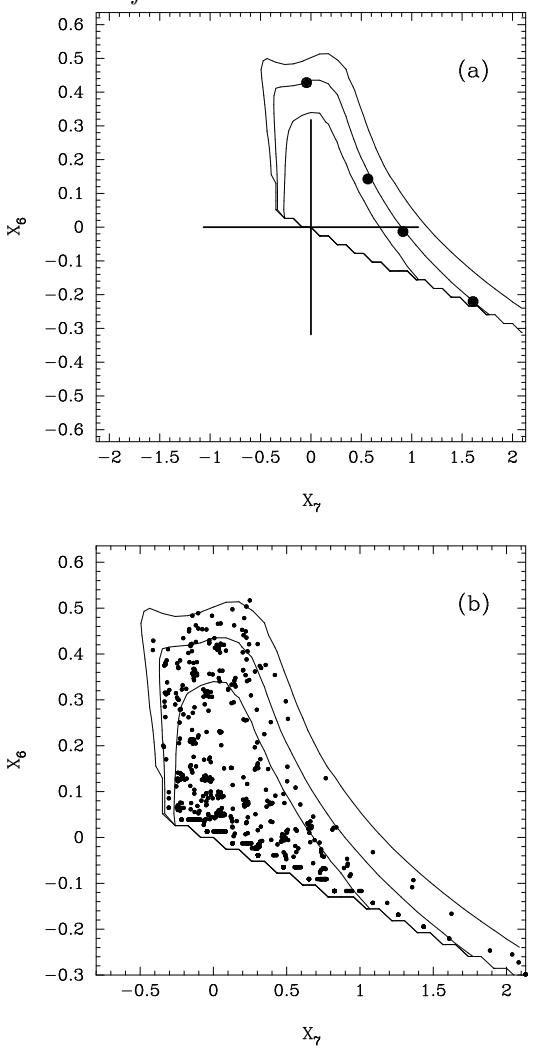

Figure 8. Likelihood ratio contours in the X_6-X_7 plane for the OMAP experiment (1, 2 and 3σ contours computed as described in the caption to Figure 3). The cross in Figure 8a shows the 1σ errors derived from the Fisher matrix (computed from the eigenvalues listed in Table 4.1). The four filled circles show the locations of the four models plotted in Figures 11 and 12 below. Figure 8b shows the maximum likelihood estimates of X_6 and X_7 for the Monte-Carlo models described in the text. These values of X_6 and X_7 were used to compute the values of the physical parameters plotted in Figure 7c.

variances of the $\mathbf{s}_i$ are dominated by a small number of principal components. In the examples given in Table 4.2, the two lowest order principal components account for most of the variance of the physical parameters. One can therefore use the principal components of the Fisher matrix to reduce the dimensionality of the parameter set to say two or three dimensions. It is then feasible to evaluate the C_ℓ's numerically on a grid in this reduced parameter space using a fast code such as CMBFAST. The numerically computed power spectra can then be used to calculate the errors on the physical parameters via a likelihood analysis in the reduced dimensional space. This procedure, although time consuming, is much faster than attempting to calculate the C_ℓ's numerically on a grid in all of the physical parameters defining the model (7 dimensions in the simplified example given above, 10 or more dimensions in the more realistic models described by BET97 and ZSS97).

Table 5: 1σ errors in estimates of cosmological parameters: comparison of Fisher matrix with exact likelihood including positivity constraints.

	OMAP		
	Fisher		Likelihood
Parameter	all	2pc	2pc
$\delta\omega_b/\omega_b$	0.082	0.061	0.032
$\delta\omega_c/\omega_c$	0.13	0.12	0.071
$\delta\omega_\Lambda$	0.094	0.091	0.052
δQ	0.013	0.0047	0.0022
δr	0.55	0.55	0.24
δn_s	0.045	0.040	0.022
δn_t	0.58	0.58	0.32
$\delta h/h$	0.11	0.11	0.064
$\delta\Omega_\Lambda$	0.19	0.18	0.15

Another consequence of the strong degeneracies among physical parameters is that the variance estimates of some parameters are extremely sensitive to imposed constraints. For example, if we restrict the range of possible models to those that have negligible tensor mode contribution (*i.e.* we constrain the parameter r to be zero) then this has a large effect on the lowest order principal components and hence on the variances of most of the physical parameters. This point will be described in more detail in Section 4.6.

4.4 Location of Doppler peaks and degeneracies for spatially flat models

In Section 3.2 we analysed the geometrical degeneracy between the parameters ω_k and ω_Λ. In this section, we analyse a similar degeneracy for spatially flat models, *i.e.* we restrict to $\omega_k = 0$ and derive the relationship between ω_Λ and ω_c (or ω_m) that leads to a nearly identical location of the Doppler peaks as a function of multipole. However, since the Doppler peak structure (heights and relative amplitudes of the peaks) depends on the matter content of the Universe, the resulting degeneracy is not exact. As we will see below, the locations of the Doppler peaks can explain the strong correlations in the ω_Λ–ω_c and h–Ω_Λ plots shown in Figure 7a. However, a precise experiment probing high multipoles such as Planck can break these degeneracies to high accuracy (*cf* Table 4.2).

The comoving wavenumber of the m'th Doppler maximum or minimum is given approximately by

$$k_m r_s(a_r) \quad = \quad m\pi \tag{16}$$

(Hu and Sugiyama 1995), where r_s is the sound horizon at recombination as defined in Section 3.2. The sound horizon is given by,

$$\begin{aligned} r_s &= \frac{c}{\sqrt{3}}\frac{1}{H_0\Omega_m^{1/2}}\int_0^{a_r}\frac{da}{(a+a_{equ})^{1/2}}\frac{1}{(1+R)^{1/2}} \\ &= \frac{c}{\sqrt{3}}\frac{a_r^{1/2}}{H_0\Omega_m^{1/2}} I_s(\omega_m,\omega_b)\,. \end{aligned} \tag{17}$$

The expression on the right hand side of this equation defines the integral $I_s(\omega_m,\omega_b)$ which is used in equation (22) below.

The parameter a_{equ} is the scale factor at the time that matter and radiation (including massless neutrinos) have equal density, and $R = (3\rho_b/4\rho_\gamma)$. Thus,

$$a_{equ}^{-1} = 24185 \left(\frac{1.6813}{1+\eta_\nu}\right)\omega_m, \qquad R = 30496\omega_b a\,. \quad (18)$$

where η_ν denotes the relative densities of massless neutrinos and photons, $\rho_\nu = \eta_\nu \rho_\gamma$, and is equal to 0.6813 for three massless neutrino flavours. Evaluating the integral in equation (17) gives,

$$r_s = \frac{4000}{\omega_b^{1/2}} \frac{a_{equ}^{1/2}}{(1+\eta_\nu)^{1/2}} \ln\left[\frac{(1+R(z_r))^{1/2} + (R(z_r)+R_{equ})^{1/2}}{1+\sqrt{R_{equ}}}\right] \text{Mpc}\,. \quad (19)$$

We define the redshift of recombination z_r as the redshift at which the optical depth to Thomson scattering is unity, assuming the standard recombination history (Peebles 1968). A useful fitting formula for z_r is given by Hu and Sugiyama (1996),

$$z_r = 1048[1 + 0.00124\omega_b^{-0.738}][1 + g_1\omega_m^{g_2}]\,, \quad (20)$$
$$g_1 = 0.0783\omega_b^{-0.238}[1 + 39.5\omega_b^{0.763}]^{-1}\,,$$
$$g_2 = 0.560[1 + 21.1\omega_b^{1.81}]^{-1}\,.$$

The locations of the Doppler peaks are therefore given by

$$\ell_m \approx m\pi \frac{d_A(z_r)}{r_s}, \quad (21a)$$

where d_A is the angular diameter distance to the last scattering surface

$$d_A = \frac{c}{H_0 \Omega_k^{1/2}} \sinh(\omega_k^{1/2} y)\,, \quad (21b)$$

and y is given by equation (8b). In fact, equation (21a) is approximate because the exact numerical coefficient relating ℓ_m and d_A/r_s depends on the projection of the three-dimensional temperature power spectrum to a two-dimensional angular power spectrum. The exact relation depends therefore on the shape of the primordial power spectrum and on the Doppler peak number m (see *e.g.* Hu and White 1996). From the numerical computations of C_ℓ we find that the location of the maximum of the first Doppler peak for a scale-invariant primordial spectrum of scalar fluctuations is well approximated by the expression

$$\ell_D \approx 0.746\pi\sqrt{3}(1+z_r)^{1/2} \frac{\omega_m^{1/2}}{\omega_k^{1/2}} \frac{\sinh[\omega_k^{1/2} y]}{I_s(\omega_m, \omega_b)}. \quad (22)$$

Equation (22) is valid for negatively curved models, though we specialize to spatially flat models in this section. To derive degeneracy lines for spatially flat models, we take the limit $\omega_k \to 0$ in equation (22). For a fixed value of ω_b, the condition of fixed ℓ_D in equation (22) then leads to a relation between ω_Λ and ω_c. Figure 9 shows the degeneracy lines for a spatially flat universe with the baryon density of our target model ($\omega_b = 0.0125$).

As in Section 3.3, for small variations of the parameters around those of the target model, we can derive the degeneracy lines by differentiating ℓ_D. We do not expect the degeneracy lines derived in this way to be exact because the degeneracies involve the entire Doppler peak structure accessible to the experiment, not just the position of the first Doppler peak. However, provided the baryon density is determined to high precision from the experiment (*i.e.* ω_b in equation 22 is held fixed), we would expect that the positions of Doppler peaks would define the degeneracy lines in the ω_c–ω_Λ plane quite accurately. These are given by

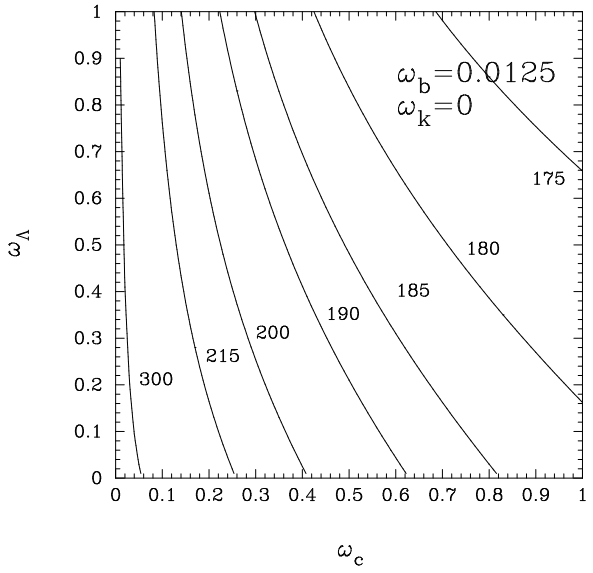

Figure 9. The position of the first Doppler peak, ℓ_D, for a spatially flat universe ($\omega_k = 0$) and assuming $\omega_b = 0.0125$. The lines show contours of constant ℓ_D, computed from equation (23a,23b), plotted as a function of ω_Λ and ω_c. The value of ℓ_D is given next to each contour.

$$\omega_c = (\omega_c)_t + b\omega_\Lambda, \qquad b = -\frac{(\partial\ell_D/\partial\omega_\Lambda)_t}{(\partial\ell_D/\partial\omega_c)_t}\,, \quad (23a)$$

where the subscript t denotes that quantities evaluated assuming the parameters of the target model. For our spatially flat target model, $b = -0.368$. As in the derivation of equation (12), the Hubble constant is degenerate with Ω_λ according to

$$h = \frac{h_t}{(1-(1+b)\Omega_\Lambda)^{1/2}}. \quad (23b)$$

The solid lines in the ω_Λ–ω_c and h–Ω_Λ panels in Figure 7 are computed from equations (23a,23b). As expected, they give a good approximation to the degeneracy lines, but the agreement is not exact.

4.5 Height of the first Doppler peak and parameter degeneracies

In analogy with the location of the Doppler peaks, the height of the first Doppler peak can provide some further insight into parameter degeneracies. The scalar component of the power spectrum can be roughly approximated by the following expression

$$\frac{\ell(\ell+1)C_\ell}{6C_2} \approx \frac{\ell(\ell+1)}{6} \frac{\Gamma(\ell + \frac{(n_s-1)}{2})}{\Gamma(\ell + \frac{(5-n_s)}{2})} \frac{\Gamma(\frac{(9-n_s)}{2})}{\Gamma(\frac{(3+n_s)}{2})}$$

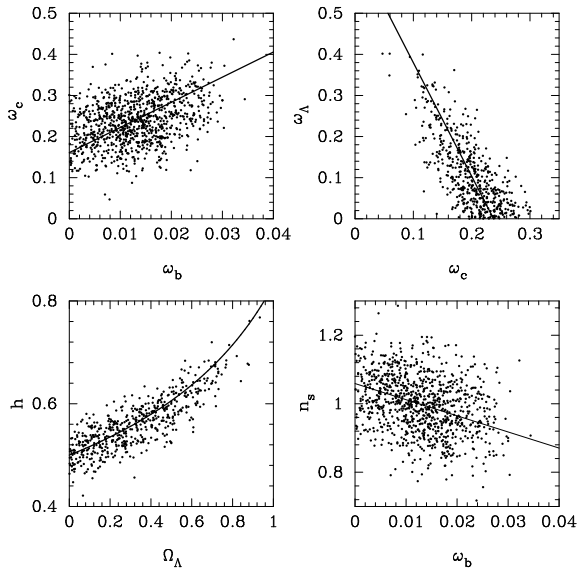

Figure 10. Simulations of parameter estimation for an experiment sampling only the first Doppler peak. We assume that the experiment is cosmic variance limited over the multipole range $2 \leq \ell \leq 300$. The solid lines in the ω_Λ–ω_c and h–Ω_Λ planes show lines of constant peak location as given by equations (23a,)23b. The dashed lines in the ω_c–ω_b planes and in the n_s–ω_b plane show lines of constant Doppler peak height as given by equation 24a.

$$+\frac{A(\omega_b,\omega_c,n_s)}{[1+(\frac{\ell_D}{8\ell})^{3/2}]}\exp\left[-\frac{(\ell-\ell_D)^2}{2(\Delta\ell_D)^2}\right]\,, \tag{24a}$$

where

$$\Delta\ell_D = 0.42\ell_D, \tag{24b}$$

$$\ln A(\omega_b,\omega_c,n_s) \approx 4.5(n_s-1)+a_1+a_2\omega_c^2+a_3\omega_c + \tag{24c}$$

$$a_4\omega_b^2+a_5\omega_b+a_6\omega_b\omega_c\,, \tag{24d}$$

$$a_1 = 2.376, a_2 = 3.681, a_3 = -5.408,$$

$$a_4 = -54.262, a_5 = 18.909, a_6 = 15.384.$$

and ℓ_D is given by equation (22) The first term in equation (24a) is the usual Sachs-Wolfe expression for a power-law fluctuation spectrum (see *e.g.* Bond 1996). The second term is a fit to the first Doppler peak determined from a grid of CMBFAST computations of C_ℓ.

The main parameter degeneracies for an experiment sampling only the multipole range $\ell \lesssim$ 300-400 will be determined by the properties of the first Doppler peak. Thus, the Doppler peak position ℓ_D will determine the degeneracy between ω_Λ, ω_c and ω_b (as described in the previous section) and the Doppler peak height will determine the degeneracies among ω_b, ω_c and n_s. This is illustrated in Figure 10, which shows a similar plot to Figure 7a, but for an experiment that is cosmic variance limited for the multipole range $2 \leq \ell \leq 300$. The conditions of constant peak height and location provide a good description of the parameter degeneracies in this case.

The situation is more complicated for a MAP or Planck type experiment because they are sensitive to the subsidiary Doppler peak structure. This is illustrated by the ω_c–ω_b scatter plot in Figure 7a. To a reasonable approximation, the subsidiary Doppler peaks pin down the value of ω_b to high accuracy and so the first principal component is almost vertical in the ω_c–ω_b plane (in fact it is tilted to a slightly negative slope to reduce the scatter in the Doppler peak locations). In this case, the condition of constant first Doppler peak height (plotted as the dashed line) determines the scatter in the orthogonal direction to that defined by the first principal component.

4.6 Constraints on the Tensor Component

Figure 11 shows the temperature power spectra for the four models indicated by the dots in Figure 8a. These models lie on the 2σ contour in the plane defined by the lowest order principal components. An experiment with the OMAP parameters can therefore only marginally distinguish these models from our target model. Figure 11 is designed to illustrate the following points:

[1] The parameters for these models are given in the upper panels. Notice that the the tensor parameters n_t and r vary by large amounts and that the most obvious differences with the power spectrum of the target model are at low multipoles. This is expected because the poorly determined tensor parameters carry high weight in the lowest two principal components (*c.f.* Table 4.2).

[2] The dotted lines in the upper and lower panels show the power spectra computed from the first derivatives according to equation (13). These differ significantly from the numerical computations (shown as the dashed lines) because the variations in n_t and r, and of some other parameters, are so large that the first order Taylor expansion breaks down. This is why the exact likelihood analysis shown in Figure 7c differs from the Fisher matrix approximation used to derive Figure 7b. The exact analysis leads to tighter constraints on the physical parameters because the first order approximation tends to underestimate the differences in the power spectra.

[3] Throughout this paper, we have allowed the parameters n_s, n_t and r to vary independently of each other. In other words, we have not imposed any additional constraints on the physical mechanism which gave rise to the fluctuations, other than that they are Gaussian characterised by power-law spectra. However, wide classes of inflationary models lead to constraints between the scalar and tensor component (see the comprehensive review by Lidsey *etal* 1997 and references therein). Such constraints can severely limit the allowed area in the plane defined by the lowest two principal components, and since these account for such a large proportion of the variance of *all* the physical parameters, the parameter errors will be extremely sensitive to these constraints.

We will investigate this last point in the remainder of this Section, using as examples two limiting constraints. It is useful first to review some key results concerning the scalar and tensor perturbations predicted by inflationary models to motivate these approximations.

Tensor perturbations, arising from quantum noise in the gravitational wave degrees of freedom, obey a perturbation equation like that of a free massless field, whereas the equation for scalar curvature fluctuations have extra terms determined by the shape of the scalar field potential $V(\phi)$, where ϕ is the inflaton field that drives inflation. The relationship between the two is therefore model dependent, and can be quite complex if $V(\phi)$ is, *e.g.*, if inflation involves more than

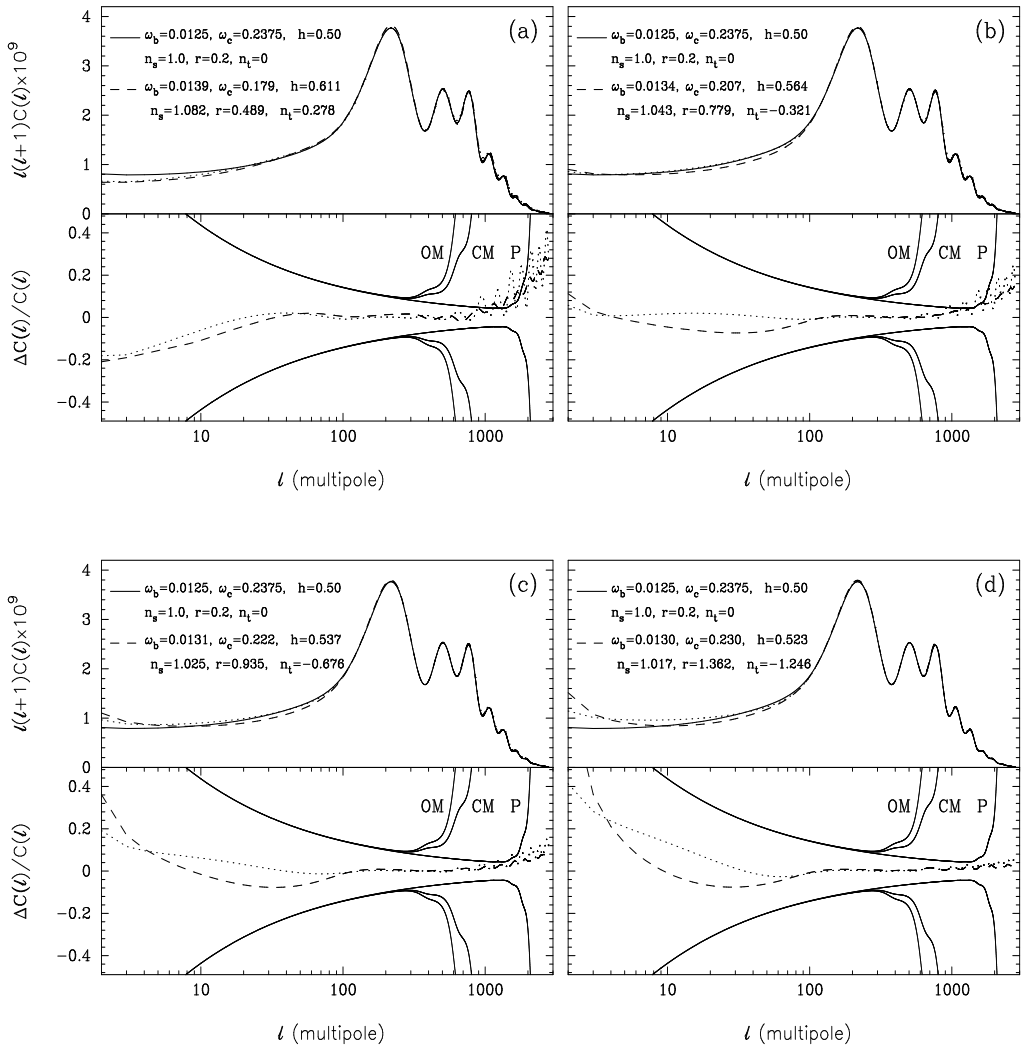

Figure 11. Temperature power spectra for the four models plotted as the filled circles in Figure 8a. For these models the two least well determined principle components X_6 and X_7 lie on the 2σ contour in Figure 8a. The physical parameters of these models are given in each panel. The solid line in the upper panel in each figure shows the power spectrum of the target model; the dashed line shows the exact computation of C_ℓ using CMBFAST for the parameters defined by X_6 and X_7. The dashed line shows C_ℓ inferred from the derivatives of C_ℓ (equation 15). The lower panels show the residuals of these curves with respect to the target model; dashed lines show the residuals for the numerical computations of C_ℓ and dotted lines show the residuals of the derivative approximation. The lines labelled OM, CM and P show the 1σ errors computed from equation (5a) for the parameters of OMAP, CMAP and Planck given in Table 2.

one dynamically important scalar degree of freedom. The essential features of inflation for one degree of freedom can be understood using a Hamilton-Jacobi formulation (Salopek and Bond 1990) in which the Hubble parameter $H(\phi)$ is treated as a function related to $V(\phi)$ by

$$H^2 \quad = \quad \frac{8\pi}{3m_p^2}\left[\frac{1}{2}\left(\frac{m_p^2}{4\pi}\frac{\partial H}{\partial\phi}\right)^2 + V(\phi)\right], \tag{25}$$

where m_p is the Planck mass. The amplitudes of the post-inflation scalar and tensor fluctuation spectra, P_S and P_T, can be expressed in terms of the value of H when a comoving wavenumber k crosses the Hubble radius $k = Ha$ at time τ_k:

$$P_S(k) = \frac{1}{1+q}\frac{H^2(\tau_k)}{\pi m_p^2}e^{2u_s}, \tag{26a}$$

$$P_T(k) = \frac{8H^2(\tau_k)}{\pi m_p^2}e^{2u_t}\,. \tag{26b}$$

The deceleration parameter q is related to the slope of H by

$$(1+q) \quad = \quad \frac{m_p^2}{4\pi}\left(\frac{\partial \ln H}{\partial\phi}\right)^2 \tag{27}$$

(e.g., Bond 1996). The parameters u_s and u_t (e.g., Bond 1994) turn out to be small for power-law like potentials (but testing whether they are non-zero is an important goal of CMB measurements). Thus the ratio of tensor to scalar power is largely determined by $(1+q)$, which measures the departure from pure exponential expansion during inflation.

Taking logarithmic derivatives of the spectra P_S and P_T with respect to wavenumber k gives the scalar and tensor

spectral indices n_s and n_t introduced in Section 3,

$$n_s = 1 + 2\left(1+\frac{1}{q}\right) - \frac{1}{q}\frac{m_p^2}{2\pi}\frac{\partial^2 \ln H}{\partial\phi^2} + \epsilon_s, \quad (28a)$$

$$n_t = 2\left(1+\frac{1}{q}\right) + \epsilon_t, \quad (28b)$$

where the terms ϵ_s and ϵ_t are small corrections arising from derivatives of u_s and u_t. Thus the difference $n_s - 1 - n_t$ is determined by the change in q over the k range appropriate for large scale structure and the CMB, which turns out to correspond to quite a narrow section of the inflaton potential. The familiar 'slow rollover' approximation assumes $q \approx -1$ in equation (25), giving $H^2 \approx 8\pi V/(3m_p^2)$, but not in equation (26a) nor in equations (28a,28b). Indeed for inflation to end, the universe must enter a deceleration phase, so realistic potentials must give departures from pure scale-invariant spectra, possibly large but more plausibly small.

The ratio of the scalar and tensor components can also be computed in terms of the inflation parameters defined above; e.g., if n_s and n_t are assumed to be constant,

$$r = \frac{C_2^T}{C_2^S} \approx 13.7(1+q)e^{2(u_t-u_s)}e^{-0.15n_t}e^{-1.1(n_s-1-n_t)} \quad (29)$$

$$\approx \frac{-6.8n_t}{(1-n_t)}e^{-0.15n_t}e^{-1.1(n_s-1-n_t)} \quad (30)$$

(Bond 1996). r also explicitly depends upon parameters such as ω_Λ and ω_k.

There are two special cases we use to illustrate constraints on the tensor component. The first is nearly uniform acceleration, (so $\partial^2 \ln H/\partial\phi^2 \approx 0$),

$$n_t \approx n_s - 1, \; r \approx -6.8\frac{n_t}{(1-n_t/2)} \approx 6.8\frac{(1-n_s)}{(3-n_s)/2} \quad (31a)$$

Pure power law expansions have q precisely constant whereas chaotic inflation models with smoothly varying power law potentials have q nearly uniform, but the deviations from $n_s - 1 \approx n_t$ are important to include if n_t is small. Equation (31a), often approximated by $r \approx 7(1-n_s)$, has been discussed by many authors (see *e.g.* Lidsey *et al.* 1997, and the footnote in Section 3.1). The second constraint we consider has

$$n_t \approx 0, \qquad r \approx 0, \quad (31b)$$

which applies to models such as 'natural inflation' (Adams *et al.* 1993) in which the inflaton begins near the maximum of an extremely flat potential, so $1+q$ and the tensor mode are exponentially suppressed. Since $d(1+q)/d\phi$ cannot then be neglected, n_s can be less than unity, possibly significantly so. Similar behaviour can arise in inflationary models based on supergravity (*e.g.* Ross and Sarkar 1996). For specific classes of models, one can refine the estimates of equations (31a,31b), for example by relating the corrections $u_t - u_s$ to the spectral indices.

In Table 4.6 we show how the errors in the cosmological parameters change if we apply the constraints of equation (31a,31b). The table lists the 1σ errors computed from the Fisher matrix including positivity constraints. The columns labelled 'no const.' give the results when no constraints are applied to the tensor spectrum, *i.e.* all parameters are allowed to vary independently. The entries under this heading for OMAP are thus identical to the entries in the second column of Table 4.3. The columns labelled '$r = -7n_t$' show the results of applying the constraint (31a) and those labelled '$r = 0$' show the result of applying the constraint (31b).

As expected (see point 3 above), imposing the constraints on a OMAP-type experiment results in a significant reduction of the errors on most parameters. Even for a CMAP-type experiment, the constraints lead to large changes in the errors of some parameters, *e.g.* the fractional error in ω_D decreases by about a factor of 3, the fractional error in h decreases by a factor of 4 and the error in Ω_Λ decreases by a factor of between 2 and 3. For a Planck-type experiment, however, imposing the constraints leads to hardly any change in the parameter errors. As Table 4.1 and Figure 6 show, for a Planck-type experiment, there is almost a decoupling between the highly uncertain tensor parameters and the high order principal components.

The results of Table 4.6 show that the errors on cosmological parameters can be reduced by making certain specific assumptions concerning the inflationary model. For OMAP and CMAP-type experiments, the reduction in the errors is very significant, but at the expense of overly restricting the inflation model. Allowing full freedom in how $V(\phi)$ and thus $H(\phi)$ is structured can result in strong variations in q, with the consequence that the power ratio 26b to 26a and the indices $n_s(k)$ and $n_t(k)$ could be complex functions of the wavenumber. As might be expected, if there is complete functional freedom, the errors on the cosmological parameters become much larger (e.g., Souradeep *et al.* 1998). Such inflation models with many features over the small regime of $V(\phi)$ that the CMB can probe seem rather baroque, and constraining the potential by invoking smoothness "prior probabilities" seems perfectly reasonable. For example, a simple way that this has been included in the past is to allow the spectral indices to "run" with a logarithmic correction: $n_s(k) \approx n_s(k_s) + \alpha \ln(k/k_s)$ (Kosowsky and Turner 1995, Lidsey *et al.* 1997). Of course, in presenting the results of CMB parameter estimation, the constraints (if any) applied to the tensor mode must be spelled out precisely.

This analysis illustrates also that constraints on the tensor component derived from CMB polarization measurements, could lead to a significant improvement in the estimates of other parameters, including the baryon and CDM densities.

5 STRENGTH, SIGNIFICANCE AND CORRELATED ERRORS IN C_ℓ

The next generation of CMB satellites should lead to estimates of C_ℓ with errors dominated by cosmic variance,

$$\frac{\Delta C_\ell}{C_\ell} \approx \sqrt{\frac{2}{(2\ell+1)f_{sky}}}$$

for multipoles $\ell \sim 1000$ – 2500. At $\ell \sim 1000$, cosmic variance limits the 1σ accuracy of a measurement of C_ℓ to about 3 percent. At first sight, it might seem as though there is little point in measuring C_ℓ (and subtracting contaminating foregrounds) to a much higher accuracy than the limit imposed by cosmic variance. However, such thinking would be incorrect. The reason is related to the concepts of strength and significance in statistics (see Press *et al.* 1996) and we illus-

Table 6: 1σ errors in estimates of cosmological parameters: effect of constraining the tensor component.

	OMAP			CMAP			PLANCK		
Param.	no const.	$r=-7n_t$	$r=0$	no const.	$r=-7n_t$	$r=0$	no const.	$r=-7n_t$	$r=0$
$\delta\omega_b/\omega_b$	0.082	0.036	0.046	0.052	0.028	0.030	0.0064	0.0056	0.0056
$\delta\omega_c/\omega_c$	0.13	0.046	0.044	0.097	0.028	0.031	0.0042	0.0042	0.0039
$\delta\omega_\Lambda$	0.094	0.025	0.026	0.069	0.014	0.020	0.0030	0.0030	0.0027
δQ	0.013	0.007	0.009	0.0066	0.0047	0.0050	0.0013	0.0010	0.0011
δr	0.55	0.054	—	0.49	0.043	—	0.33	0.023	—
δn_s	0.045	0.0077	0.015	0.030	0.0061	0.0098	0.0049	0.0032	0.0042
δn_t	0.58	0.0077	—	0.56	0.0061	—	0.40	0.0032	—
$\delta h/h$	0.11	0.032	0.033	0.082	0.020	0.028	0.0045	0.0045	0.0041
$\delta\Omega_\Lambda$	0.19	0.079	0.082	0.16	0.049	0.068	0.012	0.012	0.011

trate the point with the following simple example. Imagine that we have N independent random variates, each drawn from a Gaussian with a mean and dispersion of unity. From these N random variates we can estimate the mean

$$\mu = \frac{1}{N}\sum x_i,$$

with variance

$$\mathrm{Var}(\mu) = \frac{1}{N}.$$

Thus, even though the variance on each individual point is unity, we can determine the mean to arbitrarily high precision if we have a large enough number of points, ($\mathrm{Var}(\mu) \to 0$, in the limit $N \to \infty$). We can therefore differentiate between two samples with slightly different means ($\delta\mu \ll 1$), provided we have enough points in each sample. In this example, each point has very little *strength* (since the difference in the means is much smaller that the variance) but in the limit of large samples we can detect a small difference in the means to high *significance*.

The estimation of cosmological parameters from measurements of the power spectrum is analogous to the above example. The CMB satellites will provide, via C_ℓ, measurements of 1000–3000 nearly statistically independent numbers from which we wish to determine a much smaller number (perhaps 10–20) cosmological parameters. Since we have a large number of independent points, it is possible to measure parameter differences to high significance even though the strength of each individual point is small. Furthermore, since the number of cosmological parameters that we wish to measure is much smaller than the number of independent multipoles, we must measure each C_ℓ to an accuracy that is much smaller than the cosmic variance; correlated systematic errors between the measured C_ℓ coefficients which introduces a difference in χ^2 of the order the number of *parameters* can lead to a significant bias in the cosmological parameter estimates, the exact bias depending on the nature of the correlations. We will expand on these points in the rest of this Section.

Figure 12 is designed to illustrated the concepts of strength and significance as applied to measurements of C_ℓ. The dotted curves in the upper panels of the figure show C_ℓ for a spatially flat CDM model with the parameters listed in the Figure heading. The solid lines show the power spectrum of the spatially flat target model defined in the previous Section. The parameters for the three examples in this figure were chosen so that the C_ℓ curves would be distinguishable by OMAP at about the 2σ level; in other words, we have chosen three pairs of spatially flat CDM models that would be difficult to distinguish with OMAP alone even if there were no significant systematic errors in the measurements. The three examples have been chosen so that: in Figure 12(a) the baryon and CDM densities each differ by about 12% from those of the target model, while the inflationary parameters n_s, n_t and r are almost the same as those of the target model; in Figure 12(b), the baryon density differs by 24% from that of the target model while ω_c differs by 6%; in Figure 12(c) the CDM density differs by 18% from that of the target model while ω_b differs by 4%. In the models of Figures 12(b) and 12(c), the large changes in the densities have been balanced by relatively large changes in the inflationary parameters [§]. The points in each figure show a simulated C_ℓ spectrum for each experiment, assuming the dotted curve for C_ℓ, and with errors computed from equation (5a). The lower panels show the residuals relative to the target model.

The number labelled χ^2 in each panel gives the likelihood ratio $\chi^2 = -2ln(\mathcal{L}/\mathcal{L}_{max})$, computed from equation (9). (In computing χ^2 we used $\ell_{max} = 1000$ for OMAP, $\ell_{max} = 1500$ for CMAP and $\ell_{max} = 2800$ for Planck. However, the value of χ^2 is insensitive to ℓ_{max} since the errors in C_ℓ increase exponentially at high multipoles.) The spatially flat models that we have considered are defined by 7 parameters, thus a 95% rejection of a model requires a χ^2 of ≈ 14. This is similar, by construction, to the values of χ^2 listed for OMAP. For CMAP, and particularly, Planck, the values of χ^2 are much larger, demonstrating their superior ability to distinguish between cosmological models. An experiment such as Planck can distinguish between two C_ℓ curves at a high significance level even if the differences between them are much smaller than the cosmic variance; in fact the power spectra and residuals for a pair of mod-

[§] Note that to test inflationary models at interesting levels, we would certainly want to determine the spectral index n_s to better than ± 0.05 (see *e.g.* Liddle 1997 and references therein)

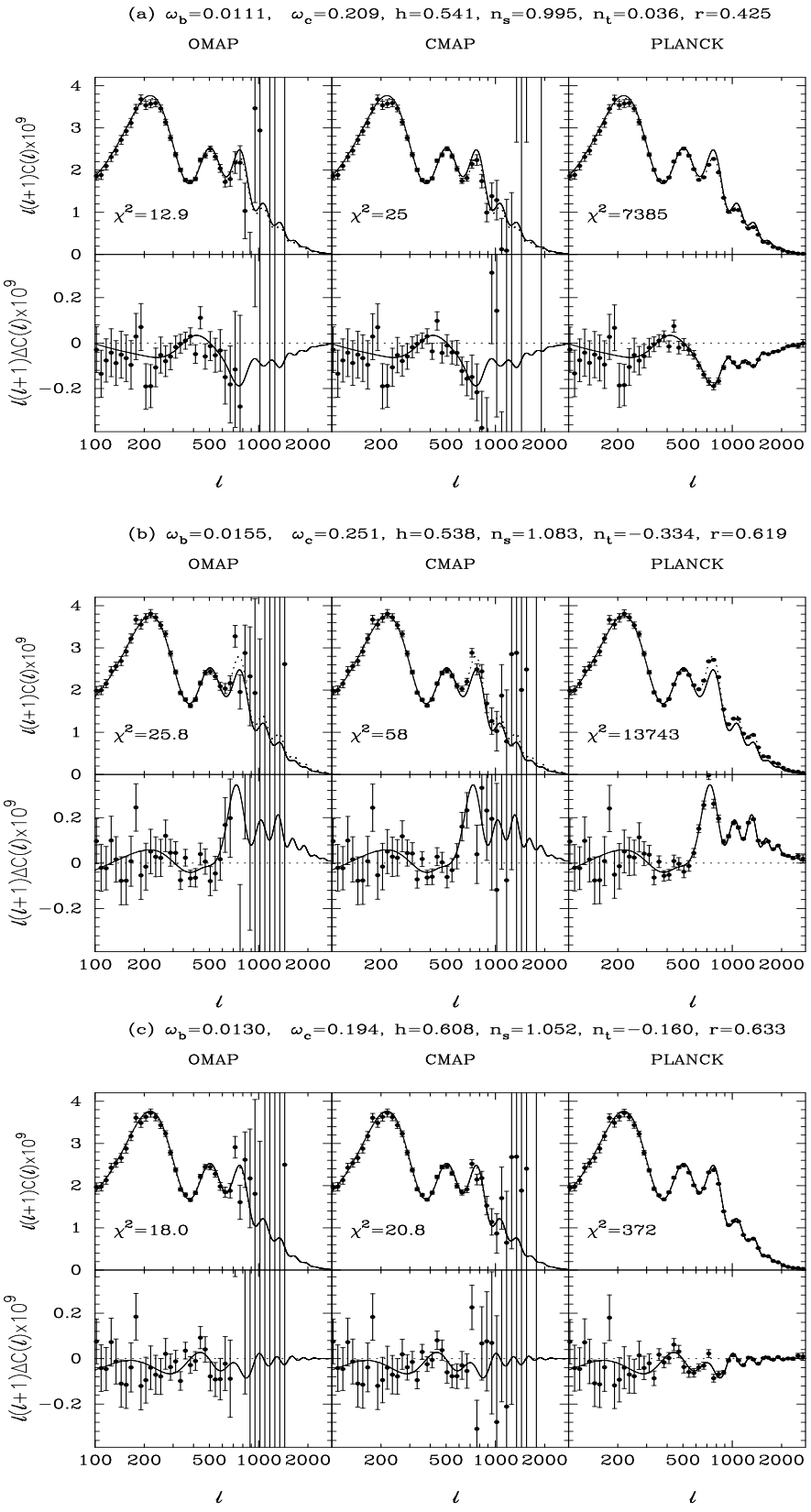

Figure 12. Temperature power spectra for three spatially flat models that are distinguishable by OMAP from the target model at about the 2σ level. The parameters for each model are listed at the top of each figure and the temperture power spectrum computed for these parameters is shown by the dashed lines in the upper panels. The power spectrum of the target model is shown by the solid lines. The filled circles and error bars show a random realization of C_ℓ for each model and 1σ errors assuming the experimental characteristics of OMAP, CMAP and Planck as listed in Table 2. The points in the lower panels show the residuals with respect to the target model. The number in each panel gives χ^2 per degree of freedom for each experiment. The points have been averaged in 100 equally spaced logarithmic intervals in ℓ over the range $3 \leq \ell \leq 3000$.

els with $\chi^2 \approx 14$ would be indistinguishable plotted on the scales of Figure 12.

Small, correlated errors in C_ℓ can thus introduce biases in estimates of cosmological parameters. The degree of bias depends on the size of the errors and the extent to which the correlated component resembles the shape of the derivatives of C_ℓ with respect to cosmological parameters. The analysis of correlated errors in C_ℓ can therefore be viewed as another aspect of the analysis of degeneracies in cosmological parameter estimation. There are many possible sources of correlated errors in C_ℓ. The most obvious are errors caused by inaccurate subtraction of emission from the Galaxy and extragalactic point sources. However, there are many other more instrument specific sources of error, for example, in a 'total-power' experiment like Planck, the scanning strategy together with instrumental '$1/f$' noise can introduce systematic errors in maps of the CMB (sometime called 'striping', Wright 1996, Bersanelli *et al.* 1996, Tegmark 1997a, Delabrouille 1998). The resulting effect of scanning on C_ℓ depends on the details of the experiment and map-making methods, but for a fairly wide class of possibilities leads to a contribution to C_ℓ that varies as $1/\ell$ (Tegmark 1997a). The scanning errors in the CMB maps should be much smaller in a differential experiment, such as MAP. Fortunately, foreground and scanning errors are unlikely to produce wiggles in C_ℓ that can distort or mimic the Doppler peak structure at high multipoles. Instead, we would expect smoothly varying errors to correlate with the low-order principal components.

To illustrate the effects of correlated errors we have constructed the following simple models

$$\frac{\ell(\ell+1)\Delta C_\ell^F}{2\pi} = A^2\ell(\ell+1)\frac{1000}{(5+\ell)^3} + B^2\frac{\ell(\ell+1)}{1000^2}, \quad (32)$$

and

$$\frac{\ell(\ell+1)\Delta C_\ell^S}{2\pi} = K^2\frac{\ell_K\ell^3(\ell+1)}{(\ell^2+\ell_K^2)^{3/2}}. \quad (33)$$

The first model (which we denote 'F') is designed to mimic the power spectrum of contaminating foregrounds. The first term is a rough approximation to the power spectrum of the major sources of Galactic emission, free-free, synchrotron and dust emission (Low and Cutri 1994; Guarini, Melchiorri and Melchiorri 1995, Tegmark and Efstathiou 1996, Bouchet *et al.* 1997) . The second term represents the white noise from unresolved extragalactic point sources. The analysis of Bouchet *et al.* (1997) suggests the following values for A and B (in μK) at 90GHz and 217GHz:

$$A = 0.36, \quad B = 1.07, \quad (90\text{GHz}), \quad (34a)$$

$$A = 1.5, \quad B = 1.39, \quad (217\text{GHz}). \quad (34b)$$

The values of A in (34a,34b) are for the cleanest regions of the sky. The second model (which we denote 'S') is based on the analysis of Tegmark (1997a) and is designed to approximate correlated scanning errors. Values for the constants K and ℓ_K are extremely sensitive to the experimental details but plausible values for a 'total-power' experiment may be $\ell_K \approx 20$ with K in the range 0.004 — $0.04\mu K$ (see Tegmark 1997a, figure 11). The models of equations (32) and (33) are illustrated in Figure 13.

Figures 14 and 15 shows the biases in a number of cosmological parameters for various choices of the parameters

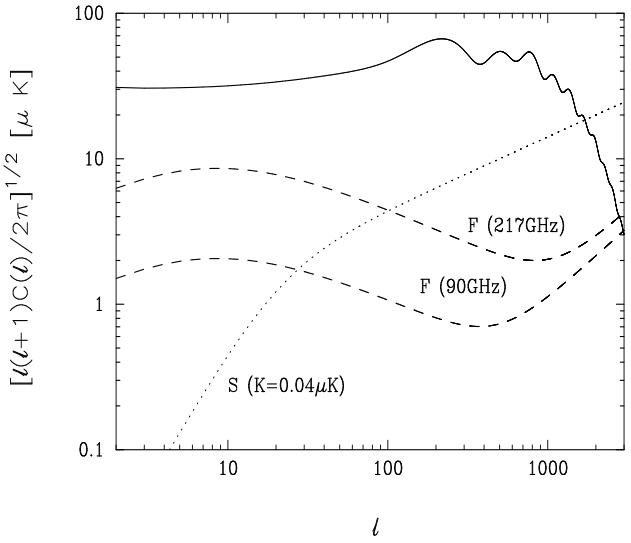

Figure 13. The solid line shows the CMB power spectrum of the spatially flat target model plotted with a logarithmic ordinate. The two dashed lines show the power spectra of the foreground model of equation (32) with the coefficients A and B set to the values appropriate for foregrounds at 90 and 217 GHz as estimated by Bouchet *et al.* (1997). The dotted line shows the scanning error model of equation (33) with $\ell_K = 20$ and $K = 0.04\mu K$.

A, B and K. To compute these figures, we have generated Monte-Carlo realizations of the CMB power spectrum, to which we have added the systematic error models of equations (32) and (33). We then compute values of the cosmological parameters by fitting the first order expansion to C_ℓ (equation 13) as in the computations of Figures 7a and 7b. The bias in each parameter has been divided by the expected standard deviation in each parameter to illustrate when systematic errors become larger than the random errors. The results are encouraging. For OMAP and CMAP, the tensor parameters are significantly affected for values of $A \gtrsim 1\mu$K and the remaining parameters for values $A \gtrsim 3\mu$K. OMAP and CMAP are unaffected by point source contributions with $B \gtrsim 10\mu$K because they are insensitive to the power spectrum at high multipoles where point sources dominate. For Planck, the systematic biases become significant for values of $A \gtrsim 1\mu$K and for $B \gtrsim 0.5\mu$K. Our analysis therefore suggests that at the highest frequencies, and in clean regions of the sky, MAP should provide unbiased estimates of cosmological parameters without any correction for foregrounds. For Planck, removal of foregrounds is likely to be required to achieve unbiased results. However, with the wide frequency coverage and high sensitivity of Planck it should be possible to remove foreground contributions to C_ℓ to an accuracy that is well below the cosmic variance errors (Tegmark and Efstathiou 1996). Even without any frequency information, it would be possible to test for biases by including parametric models of the systematic errors in the likelihood analysis.

Figure 14 shows that for Planck, low-level scanning errors could potentially lead to biases in cosmological parameters. These biases could probably be removed adequately by including a parametric model of the scanning errors derived from simulations such as those described by Delabrouille (1998). The example of Figure 14 does, however, show that

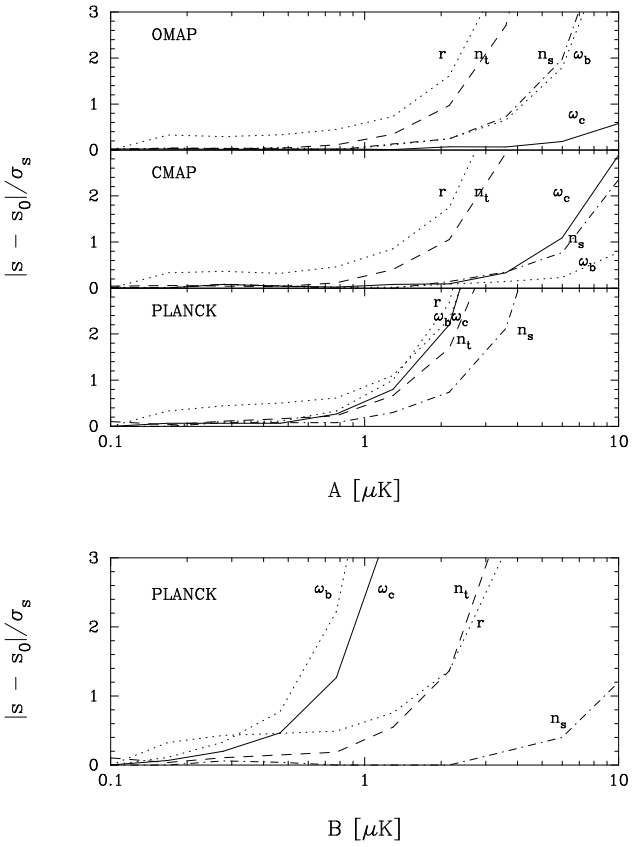

Figure 14. The absolute bias of various cosmological parameters divided by their standard errors plotted against the parameter A representing Galactic foregrounds, and B representing point sources (equation 32).

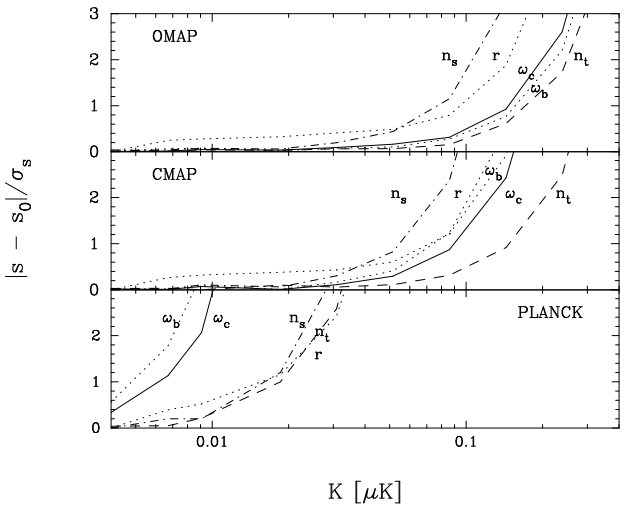

Figure 15. The absolute bias of various cosmological parameters divided by their standard errors plotted against the parameter K representing scanning errors according to equation 33.

scanning errors may be a serious concern for the analysis of Planck data.

6 EXTERNAL CONSTRAINTS AND PARAMETER DEGENERACIES

In practice, observations of the CMB anisotropies will be supplemented by other astronomical observations which can be used to remove some of the parameter degeneracies. Some of these are described in this Section. Indeed, such constraints have already been applied in some analysis of cosmological parameters. For example, Webster *et al.* (1998) describe joint likelihood analysis of CMB measurements and observations of large-scale structure. White (1998) and Tegmark *et al.* (1998) describe how CMB measurements can be combined with distances derived from Type 1a supernovae (*e.g.* Perlmutter *et al.* 1997, 1998) to remove the geometrical degeneracy.

6.1 Constraints on the Hubble Constant

If the matter content parameters ω_m and ω_D are well constrained by CMB observations, a constraint on the Hubble constant converts directly into a constraint on Ω_Λ. For our spatially flat target model, the constraint is given by equation (12) and generally,

$$\delta\Omega_\Lambda \approx 2\frac{\delta H_0}{H_0}. \tag{35}$$

A determination of Ω_Λ to an accuracy of ~ 0.1 should be possible if the systematic and random errors on the Hubble constant can be reduced to $\lesssim 5\%$, as seems feasible (see *e.g.* Freedman *et al.* 1998).

6.2 Constraints on the age of the Universe

The age of the Universe is give by the integral,

$$t_0 = 9.8\ \mathrm{Gy} \int_0^1 \frac{a\ da}{[\omega_m a + \omega_k a^2 + \omega_\Lambda a^4]^{1/2}} \tag{36}$$

(see *e.g.* Peebles, 1993, equ 13.9). If the matter content ω_m is well constrained by the CMB anisotropies, then limits on the age of the Universe can be used to constrain the geometrical degeneracy in the $\omega_\Lambda - \omega_k$ plane. This is illustrated in Figure 15. However, since the slope of the geometrical lines are so steep, the limits on ω_Λ are sensitive to the parameters of the target model. In the example shown in Figure 15, an age constraint of $t_0 \gtrsim 14$ Gyr (*e.g.* Chaboyer *et al.* 1996) would lead to a relatively weak limit of $\omega_\Lambda \lesssim 0.7$ in a spatially flat universe ($\mathcal{R} = 2$), but to tighter limits in a universe with a larger value of ω_k.

6.3 Constraints on Large-Scale Clustering

Measurements of galaxy clustering can provide constraints on the shape and amplitude of the galaxy power spectrum. These are often characterised by the *rms* amplitude of the galaxy fluctuations in spheres of radius $8h^{-1}$Mpc, $(\sigma_8)_g$, and a shape parameter Γ (see Efstathiou, Bond and White 1992). When combined with CMB anisotropy measurements, observation of galaxy clustering can constrain the distribution of mass fluctuations relative to galaxies. This information, together with constraints on redshift space anisotropies

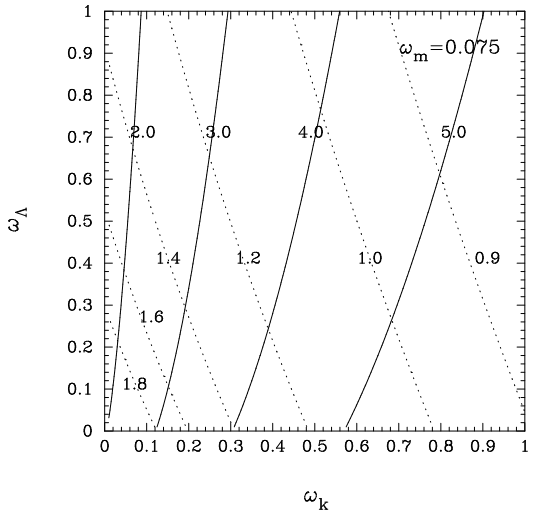

Figure 16. Analogue of Figure 1b for a model with $\omega_m = 0.075$. The solid line show constant values of $\mathcal{R}$ in the ω_Λ– ω_k plane and the dashed lines show lines of contours of equal age listed in 10 Gyr units.

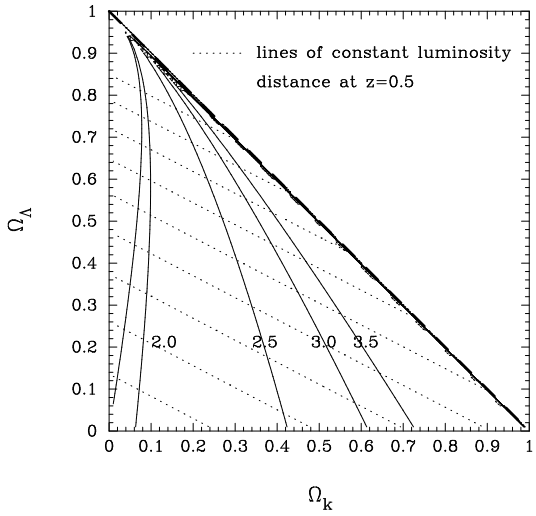

Figure 17. The solid lines show the degeneracy lines of constant $\mathcal{R}$ as plotted in Figure 1a. The dashed lines show lines of constant luminosity distance at a redshift of $z = 0.5$ in steps of $50h^{-1}$Mpc, extending from $1700h^{-1}$Mpc at the bottom of the figure to $2100h^{-1}$Mpc at the top.

and cosmic velocity fields, can be used to improve the estimates of many of the cosmological parameters described here and including the epoch of reionization (see for example Tegmark 1997b). In the future, observations of weak gravitational lensing may provide more direct estimates of the matter power spectrum (Blandford *et al.* 1991, Miralda-Escude 1991, Kaiser 1992, see Seljak 1997b for a recent discussion). If we restrict to CDM models with low baryon fractions, then the power spectrum shape parameter Γ is related to the matter density according to $\Gamma \approx \Omega_m h = \omega_m/h$ (see Eisenstein and Hu, 1998, equations 30 and 31 for a fitting function for Γ that includes the baryon density and associated scale dependence). A measurement of Γ from large-scale structure measurements can thus be combined with an accurate determination of ω_m from the CMB anisotropies to yield an estimate of the Hubble constant, and hence to constrain the cosmological constant as described in Section 6.1.

6.4 Constraints on the Geometry from Type 1a Supernovae

The distances of Type 1a supernovae at redshifts $z \gtrsim 0.5$ are already providing strong constraints on the geometry of the Universe (*e.g.* Perlmutter *et al.* 1997, 1998). Such measurements provide a potentially powerful method of removing the geometrical degeneracy in the CMB measurements. This is illustrated by Figure 16, which shows the CMB geometrical degeneracy lines in the Ω_Λ—Ω_k plane plotted as in Figure 1a. The dashed lines show constant values of the luminosity distance at $z = 0.5$[¶], approximating the slope of the error ellipses in this plane derived from supernovae measurements. To first order, standard candles such as Type 1a supernovae yield near degenerate constraints along the dashed lines. As has been noted as well by White (1998), Tegmark *et al.* (1998) and others, these intersect almost orthogonally with the CMB geometrical degeneracy lines. Type 1a supernovae thus offer an extremely powerful way of breaking the geometrical degeneracy, provided systematic errors (which move the supernova maximum likelihood almost along the geometrical degeneracy lines) can be shown to be small.

[¶] This is approximately the median redshift of the distant supernovae samples, (Ellis, private communication).

7 CONCLUSIONS

High precision observations of CMB anisotropies promise a revolution in our knowledge of fundamental cosmological parameters. In this paper we have analysed the degeneracies between cosmological parameters determined from CMB experiments, using the MAP and Planck satellites as an indication of what might be achieved in the next decade. Our conclusions are as follows:

[1] The geometrical degeneracy between Ω_Λ and Ω_k for models with identical matter content, ω_b, ω_c, ... is nearly exact and cannot be broken from observations of the linear CMB anisotropies alone. Breaking of this degeneracy requires additional data, such as distances to Type 1a supenovae, or the detection of small non-linear effects such as gravitational lensing of the CMB.

[2] Small numerical errors in calculating the CMB power spectrum C_ℓ can accumulate in computations of the Fisher matrix leading to spurious breaking of near exact degeneracies. These numerical errors can be avoided by rotating to new variables defined by the degeneracies as described in Section 3.3.

[3] The Fisher matrix for a particular experiment defines a set of principal components, *i.e.* orthogonal linear combinations of the cosmological parameters s_i defining the theoretical CMB power spectrum C_ℓ. Restricting to a spatially flat universe and an idealised set of 7 cosmological parameters,

we find that most of the variance in estimates of the s_i from the MAP satellite comes from the two lowest order (*i.e.* least well determined) principal components.

[4] The degeneracies between poorly determined and well determined parameters limits the accuracy of the Fisher matrix. An exact likelihood analysis for a MAP-type experiment shows that the Fisher matrix can overestimate the errors on even apparently well determined parameters such as ω_b by factors of two or more.

[5] For a Planck-type experiment, the principal components are almost identical to physical variables. The five highest order principal components couple strongly to ω_b, ω_c, Q, n_s and ω_Λ respectively. The two lowest order components couple strongly to the parameters r and n_t defining the tensor component.

[6] For a MAP-type experiment, the errors on the matter densities ω_b and ω_c are sensitive to theoretical constraints on the tensor and scalar fluctuation spectra (r, n_t and n_s) and hence on the nature of the inflationary model. The variances on ω_b and ω_c from a Planck-type experiment are insensitive to the details of inflation, provided the tensor and scalar fluctuation spectra are characterised by weakly scale-dependent power-laws.

[7] The lowest order principal components for an experiment sampling low multipoles ($\ell \lesssim 300$ in a spatially flat universe) can be understood in terms of the position and height of the first Doppler peak.

[8] Correlated errors in C_ℓ that are much smaller than the errors from cosmic variance can introduce significant biases in the estimates cosmological parameters. We have analysed simple models for correlated errors in C_ℓ arising from Galactic foregrounds and extragalactic point source and from scanning errors. If our simple models are correct, foregrounds should not introduce large biases in cosmological parameters estimated from CMB measurements at frequencies in the range $\approx$ 100–200GHz. However, there may be foreground components that are not included in our model and that dominate in this frequency range (*e.g.* Leitch *et al.* 1997). In this case, subtraction of the frequency dependent foregrounds from the primary anisotropies to high accuracy may be necessary to derive cosmological parameter estimates from the CMB. Scanning errors are another potential source of biases in cosmological parameter estimates. Our models suggest that scanning errors may be problematic for Planck and a more detailed analysis is evidently required before the scanning strategy is frozen.

[9] Observations of CMB anisotropies can be supplemented with more conventional astronomical measurements, such as the large-scale mass distribution, estimates of the age of the Universe and distances to Type 1a supernovae, to break the geometrical degeneracy.

ACKNOWLEDGEMENTS

We thank Max Tegmark and Francois Bouchet for useful discussions. GPE thanks PPARC for the award of a Senior Fellowship. JRB was supported by a Canadian Institute for Advanced Research Fellowship.

REFERENCES

Albrecht A. Battye R.A., Robinson J., 1997, astro-ph/9711121.
Bennett C. *et al.* 1996; MAP home page, http://map.gsfc.nasa.gov
Bersanelli, M. *et al.* 1996, COBRAS/SAMBA, The Phase A Study for an ESA M3 Mission, ESA Report D/SCI(96)3; Planck home page, http://astro.estec.esa.nl/SA-general/Projects/Cobras/cobras.html
Blandford R.D., Saust A.B., Brainerd T.G. & Villumsen J.V., 1991, MNRAS, **251**, 600.
Bond, J.R. 1996, *Theory and Observations of the Cosmic Background Radiation*, in "Cosmology and Large Scale Structure", Les Houches Session LX, August 1993, ed. R. Schaeffer, Elsevier Science Press.
Bond J.R., 1994 in *Relativistic Cosmology*, Proc. 8th Nishinomiya-Yukawa Memorial Symposium, ed. M. Sasaki, (Universal Academy Press, Tokyo), pp. 23.
Bond J.R., Efstathiou G., 1984, ApJ, **285**, L45.
Bond J.R., Efstathiou G., 1987, MNRAS, **226**, 665.
Bond J.R., Crittenden R., Davis R.L., Efstathiou G., Steinhardt P.J., 1994, Phys Rev Lett, 72, 13.
Bond J.R., Efstathiou G., Tegmark M., 1997, MNRAS, 291 L33.
Bond, J.R., Jaffe, A. 1997, in Proc. XXXI Rencontre de Moriond, ed. F. Bouchet, Edition Frontières, in press; astro-ph/9610091.
Bouchet F., Gispert R., Puget, J-L., 1995, *The mm/sub-mm Foregrounds and Future CMB Space Missions*, In Unveiling the Cosmic Infrared Background; AIP Conference Proceedings 348, Baltimore, Maryland, USA, E. Dwek (ed), p255.
Bouchet F., Gispert R., Boulanger, F., Puget, J-L., 1997, *Comparing Performances of CMB Experiments*, In Proceedings of the XVIth Moriond Astrophysics Meeting, Editiones Frontiers, Gif-sur-Yvette. F. Bouchet, R. Gispert, B. Guiderdoni, J. Trân Than Vân, (eds), p481.
Caldwell, R.R., Dave, R., Steinhardt P.J., 1998, Phys Rev Lett, 80, 1582.
Chaboyer B., Demarque P., Kernan, P.J., Krauss L.M., 1996, Science, 271, 957.
Copeland E.J., Grivell I.J., Kolb E.W., Liddle A.R., 1998, astro-ph 9802209.
Crittenden, J.R., Turok, N., 1995, Phys Rev Lett, 75, 2642.
Davis R.L., Hodges H.M., Smoot G.F., Steinhardt P.J. and Turner M.S., 1992, Phys Rev Lett, 69, 1856.
Delabrouille, J., 1998, A&A Suppl. Ser., 127, 555.
Eisenstein D.J. and Hu W., 1998, ApJ, 496, 605.
Freedman W.L., Mould J.R., Kennicutt R.C., Madore B.F, 1998, Invited Review at IAU Symposium No 183, Kyoto, Japan, astro-ph/9801080.
Hancock, S., Rocha G., Lasenby A.N., Gutierrez C.M., 1997, MNRAS, in press, astro-ph 9708254.
Hobson M.P., Jones A.W., Lasenby A.N., Bouchet F.R. 1998, MNRAS submitted.
Hu W, Sugiyama N, 1995, Phys Rev D50, 7173.
Hu W, White M., 1996, ApJ, 471, 30.
Hu W, Sugiyama N, Silk J, 1997, Nature, 386, 37.
Jungman G., Kamionkowski M., Kosowsky A., Spergel D.N. 1996 Phys. Rev. D54, 1332.
Kaiser N., 1983, MNRAS, **202**, 1169.
Kaiser N., 1992, ApJ, **388**, 272.
Kamionkowski M., Kosowsky A., 1998, Phys Rev D57, 685.
Kendall, M.G., 1975, *Multivariate Analysis*, Griffin, London.
Knox L., 1995 Phys. Rev. D52, 4307.
Knox L., Turner M.S., 1994 Phys. Rev. Lett., 73, 3347.
Leitch E.M., Readhead A.C.S., Pearson T.J., Myers S.T., 1997 ApJ, 486, 23L.
Liddle A.R., Lyth D.H., 1992 Phys Lett, B291, 391.
Lidsey J.E., Liddle A.R., Kolb E.W., Copeland E.J., Barreiro, T.,

Abney M., 1997 RMP, 69, 373.
Linde A. 1990, *Particle Physics and Inflationary Cosmology*, Harwood Academic Publishers.
Lineweaver, C.H., Barbosa D., 1998a, ApJ, in press, astro-ph9706077.
Lineweaver, C.H., Barbosa D., 1998b, A&A, 329, 799.
Miralda-Escude J., 1991, ApJ, 380, 1.
Peebles P.J.E., 1968, ApJ, 153, 1.
Peebles P.J.E., 1993, *Principles of Physical Cosmology*, Princeton University Press, Princeton, New Jersey.
Perlmutter S, et al., 1997, ApJ, 483, 565.
Perlmutter S, et al., 1998, Nature, 391, 51.
Press W.H., Flannerry B.P., Teukolsky S.A., Vetterling W.T., 1986, *Numerical Recipes*, Cambridge University Press, Cambridge.
Ratra B., Peebles P.J.E., 1988, Phys Rev D 37, 3406.
Ross G.G., Sarkar, S., 1996, Nucl. Phys. B461, 597.
Salopek D.S., Bond J.R., 1990, Phys. Rev. D42, 3936.
Seljak U., 1997a, ApJ, 482, 6.
Seljak U., 1997b, astro-ph/9711124.
Seljak U., Zaldarriaga M. 1996, ApJ, 469, 437.
Souradeep, T, Bond J R, Knox L, Efstathiou G, Turner M S 1998 astro-ph/9802262
Tegmark M., 1997a, Phys Rev. D56, 4514.
Tegmark M., 1997b, Phys Rev. Lett, 79, 3806.
Tegmark, M., Taylor, A. Heavens, A. F. 1997, ApJ, 480, 22.
Tegmark, M., Eisenstein D.J., Hu W., Kron R.G., 1998, astro-ph/9805117.
Tegmark M., Efstathiou G., 1996, MNRAS, **281**, 1297.
Turok, N, Pen, U., Seljak U., 1997, astro-ph/9706250.
Webster M., Hobson M.P., Lasenby A.N., Lahav O., Rocha, G., 1998, astro-ph/9802109.
Wright E.L., 1996, *Scanning and Mapping Strategies for CMB Experiments*, Paper presented at the Data Analysis Workshop in Princeton 22 Nov 1996, astro-ph/9612006.
Zaldarriaga, M., Spergel D.N., Seljak U., 1997 ApJ, 488, 1.